

UAV-aided Radio Map Construction Exploiting Environment Semantics

Wenjie Liu and Junting Chen

School of Science and Engineering (SSE)

Future Network of Intelligence Institute (FNii)

The Chinese University of Hong Kong, Shenzhen, Guangdong 518172, China

Abstract

This paper constructs a full dimensional (6D) radio map to predict the channel gain between any transmitter location and any receiver location based on received signal strength (RSS) measurements between low-altitude aerial nodes and ground nodes. The main challenge is how to describe the signal strength attenuation due to the blockage from the environment. Conventional interpolation-type approaches fail to exploit the close relation between the radio map and the geometry of the environment. This paper proposes to construct radio maps by first estimating and constructing a multi-class 3D virtual obstacle map that describes the geometry of the environment with radio semantics. Mathematically, a least-squares problem is formulated to jointly estimate the virtual obstacle map and the propagation parameters. This problem is found to have a partial quasiconvexity that leads to the development of an efficient parameter estimation and radio map construction algorithm. Numerical experiments confirm that the proposed method substantially reduces the amount of measurement required for achieving the same radio map accuracy. It is also demonstrated that in a unmanned aerial vehicle (UAV)-aided relay communication scenario, a radio map assisted approach for UAV placement can achieve more than 50% capacity gain.

Index Terms

Radio map, environment-aware, radio semantics, unmanned aerial vehicle (UAV)

I. INTRODUCTION

It becomes increasingly important for wireless communication networks to learn about the communication environment. For example, millimeter-wave, terahertz, and integrated aerial and terrestrial communications favor a line-of-sight (LOS) propagation condition. Thus, knowing the radio environment and even the geometry of the surrounding may help user selection, beamforming, and position optimization for communication nodes [1]–[4]. A recent trend is to leverage *radio maps* for optimizing communication networks, where a radio map

is a data model that captures the location-dependent wireless channel quality between a transmitter and a receiver [5]–[8].

Recent studies have exploited radio maps for unmanned aerial vehicle (UAV) position optimization and trajectory planning for data harvesting, blockage-aware wireless power transfer, and network localization [2]–[8]. For example, in a typical scenario of UAV-to-ground communication in dense urban environment, there are buildings and trees that probably appear at arbitrary locations and block the air-to-ground signal. Most earlier works addressed this issue using a *probabilistic* model, which describes the probability of the LOS condition as a function of the elevation angle at the ground node [9], [10]. By contrast, radio map based models can adapt to specific geography environments and determine the actual location-dependent LOS condition and channel gain. Some recent study on the UAV relay communication further revealed that, when a radio map is partially available, the throughput performance of a position-optimized UAV relay network can be substantially enhanced as compared to the methods based on probabilistic models [2], [7], [8].

However, little is known on how to efficiently construct a radio map. The following challenges need to be addressed. First, it usually requires a huge amount of measurement data for radio map construction due to the ample degrees of freedom for a propagation channel. A *full* dimensional radio map for a narrowband single antenna system may still need 6 dimensions to describe the channel quality between any transmitter location and any receiver location in 3D. Second, it is also costly to store, transfer, and share radio maps among communication nodes. Third, it is essential, yet challenging, to embed the environment information to radio maps as wireless channels depend on the geography environment via a complicated mechanism involving signal reflection, diffraction, and scattering. As to be discussed below, pure data-driven environment-blind approaches may result in low efficiency of utilizing the measurement data; classical channel models, such as the simplified probabilistic LOS model, may suffer from poor prediction performance; and ray-tracing methods suffer from the overwhelming requirement for computing capability and high precision city map information.

This paper attempts to build a full dimensional radio map from received signal strength (RSS) measurements between scattered low altitude aerial nodes and ground nodes. The core idea is to reconstruct the geometry of the propagation environment with *radio semantics* embedded, such that one can infer whether the propagation is under LOS, slightly obstructed, or in deep shadow, and exploit this information to predict the channel gain between any two wireless nodes. Specifically, we build a multi-class 3D environment model, where the

environment does *not* necessarily represent the visual appearance of buildings, but it is a model that captures the *semantic* meaning of how the signal strength will be affected by the surrounding. For instance, a pillar made of plastic may impose less attenuation on radio signals than a concrete pillar may do. Mathematically, we construct multi-class 3D virtual obstacles to describe the propagation environment for any pair of wireless nodes in 3D, and based on this, we construct an environment-aware radio map. We show that the proposed approach not only reconstructs the geometry of the propagation environment, but also achieves better accuracy in radio map construction than conventional interpolation-type methods. Moreover, as the information is compressed in the proposed multi-class 3D virtual obstacle model, it becomes easier to convey and share radio maps in the network.

A. Related Work

Data-driven approaches: Radio maps have been studied a lot for indoor localization [11], [12]. In these scenarios, the radio signatures are sampled through RSS measurement over a 2D area, and the focus there was to handle sparsity and interpolate the measurement data. Some of these methods include k -nearest neighbor (KNN) [13], [14], sparse matrix or tensor processing [12], and Kriging [15], [16]. Based on the recent advance of image processing, deep learning for radio map construction was also investigated in [17]–[21]. Note that these approaches were mainly designed for 2D radio maps, and they may not be easily extended to our scenario of interest.

Model-based approaches: Conventional channel models first label the local area into fine categories, such as urban and sub-urban, and then select a parametric model from the fine category [9], [10]. From the view of signal propagation, some works [22], [23] classify signals into LOS and non-line-of-sight (NLOS) and then adopts path loss model with a city map model. However, the limitation is that the categorization is usually objective, and there are usually a limited number of predefined models and sets of parameters to choose from.

Ray-tracing: These methods are based on the 3D model of the environment and compute the physical propagation paths through analyzing any possible reflection, diffraction, and scattering [24], [25]. However, they are not only computationally expensive but also very sensitive to the precision and the accuracy of the information available, including the fine 3D model of the structure and its material.

B. Our Contributions

The paper aims at addressing the following two main issues:

- *How to model the radio map with the geometry of radio environment embedded;*
- *How to develop efficient algorithms to construct both the 3D environment and the radio map.*

We develop a radio map model that consists of a multi-class 3D virtual obstacle model to capture the geometry of the radio environment. The key intuition is that if a link is relatively weak considering its propagation distance, then there should be one or more obstacles that block the direct path of the link. With the proposed model, the radio map construction problem is transformed into a joint estimation problem of the propagation parameters and the location and height of the 3D virtual obstacles. A 3D city map is *not* required, although it can help better initialize the algorithm.

Our earlier work [26] clusters the measurement into different propagation conditions, such as LOS and NLOS, and the follow-up work [27], [28] designs a preliminary virtual obstacle model based on the estimated LOS labels. However, the existing approach is an open-loop method, where if the LOS label obtained from [26] were wrong, the error would propagate and be magnified in the subsequent steps in [27]. In this paper, we circumvent this limitation by developing a new model and new algorithm to estimate the *virtual obstacle map* directly from the measurement data.

The novelty and contribution are summarized as follows:

- We develop a novel radio map model that consists of a parametric sub-model that captures the geometry of the propagation environment with radio semantics and a non-parametric sub-model that captures the residual of the shadowing. With such a framework, the model performs well with both small or large amount of training data.
- We formulate a least-squares estimation problem for the radio map construction. While the problem is non-convex with degenerated gradient, we discover and prove the *partial quasiconvexity* of the problem; based on this theoretical result, we develop an efficient algorithm to construct the radio map as well as the geometry of the virtual environment.
- We conduct numerical experiments to verify that the proposed approaches significantly outperform KNN and Kriging for radio map construction using the city data of Shanghai. With the reconstruction of the geometry of the virtual environment, we also demonstrate the performance advantage of applying the proposed radio map model to UAV-assisted wireless communication.

The rest of the paper is organized as follows. In Section II, the multi-degree channel and multi-class virtual obstacle model are established. Section III and Section IV develop the

algorithm and establish theoretical results. Two applications and their numerical results are demonstrated in Section V. Conclusions are drawn in Section VI.

II. RADIO MAP MODEL

Consider wireless communications between a ground user and a low altitude aerial node over a dense urban environment. Typically, the aerial node can be a relay base station (BS) carried by a UAV or a sensing device installed on a high tower or on the rooftop. The focus of this paper is to construct a radio map to characterize the channel gain between every terrestrial (ground) user position \mathbf{p}_u and every aerial node (drone) position \mathbf{p}_d pair based on a limited number of measurement samples, where $\mathbf{p}_u, \mathbf{p}_d \in \mathbb{R}^3$.

A. Radio Map with Environment Semantics

Denote the *communication link* $\mathbf{p} = (\mathbf{p}_u, \mathbf{p}_d) \in \mathbb{R}^6$ as the positions of the ground user and aerial node pair. The signal that propagates between \mathbf{p}_u and \mathbf{p}_d consists of multiple paths which experience penetration, reflection, diffraction, and scattering according to the specific environment. We aim at building a radio map $g(\mathbf{p})$ to capture the large-scale effect of the channel gain, including the path loss and the shadowing for each link characterized by the 6-dimensional location \mathbf{p} .

Recall a classical channel model $\sum_{k=0}^1 (\beta_k + \alpha_k \log_{10} \|\mathbf{p}_u - \mathbf{p}_d\|_2) \mathbb{I}\{\mathbf{p} \in \mathcal{D}_k\} + \xi$, which is based on the 0-1 categorization of links being in the LOS region $\mathbf{p} \in \mathcal{D}_0$ or in NLOS region $\mathbf{p} \in \mathcal{D}_1$; and ξ is a random variable for the shadowing. We extend such a classical model to a $(K+1)$ -degree model with soft categorization. Specifically, the proposed radio map model $g(\mathbf{p})$ consists of a *deterministic radio map* $\bar{g}(\mathbf{p}; \boldsymbol{\theta}, \mathbf{H})$ and a *residual shadowing map* $\xi(\mathbf{p})$:

$$g(\mathbf{p}) = \bar{g}(\mathbf{p}; \boldsymbol{\theta}, \mathbf{H}) + \xi(\mathbf{p}) \quad (1)$$

where the deterministic radio map

$$\bar{g}(\mathbf{p}; \boldsymbol{\theta}, \mathbf{H}) \triangleq \sum_{k=0}^K (\beta_k + \alpha_k \log_{10} \|\mathbf{p}_u - \mathbf{p}_d\|_2) S_k(\mathbf{p}; \mathbf{H}) \quad (2)$$

is parameterized by $\boldsymbol{\theta} = \{\alpha_k, \beta_k\}_{k=0}^K$ for each path loss sub-model $\beta_k + \alpha_k \log_{10} \|\mathbf{p}_u - \mathbf{p}_d\|_2$ under different degrees of signal obstruction; the term $S_k(\mathbf{p}; \mathbf{H})$ models the likelihood that link \mathbf{p} experiences in the k th degree of signal obstruction with parameter \mathbf{H} , to be explained in the next subsection, to capture the semantic information of the propagation environment. The component $\xi(\mathbf{p})$ is a random process assumed with zero mean and bounded variance.

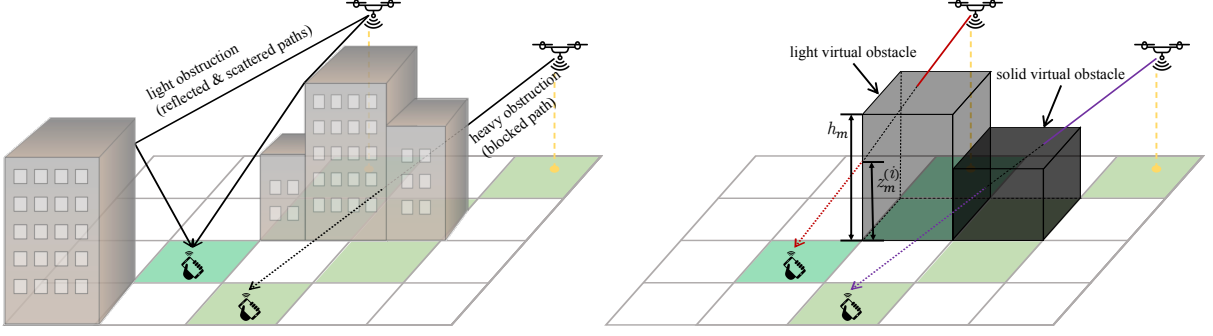


Figure 1. Left: the multi-path propagation in reality; right: a virtual obstacle structure that captures the semantic information of the propagation environment.

The advantage of the proposed model (1) is as follows: First, as suggested by measurement data that there are rarely sharp edges between LOS and NLOS, a probabilistic function $S_k(\mathbf{p}; \mathbf{H})$ approximates the reality better than an indicator function does in a classical model. Second, intuitively, the more segments \mathcal{D}_k to estimate, the more precise the model $\bar{g}(\mathbf{p}; \boldsymbol{\theta}, \mathbf{H})$ may approximate the reality, resulting in a lower variance for the random component $\xi(\mathbf{p})$. Third, the geometry of the radio propagation environment will be explicitly built into the model $\bar{g}(\mathbf{p}; \boldsymbol{\theta}, \mathbf{H})$ to assist radio map reconstruction, as to be shown later.

B. Virtual Obstacle Model

We propose to impose a *multi-class virtual obstacle model* for $S_k(\mathbf{p}; \mathbf{H})$, the likelihood of \mathbf{p} being in the k th propagation region \mathcal{D}_k to describe the environment semantics. The general idea is to employ an *equivalent* virtual obstacle at a certain *location*, with appropriate *height* and *type* to intersect with the direct path \mathbf{p} to represent the likelihood $S_k(\mathbf{p}; \mathbf{H})$. Hence, the virtual obstacle may not be mapped to a building in the reality, but serves as a geometry representation of the radio propagation environment.

For example, as illustrated in Fig. 1, if a link \mathbf{p} is in deep shadow, then we place a solid virtual obstacle to intersect the direct path of \mathbf{p} ; on the other hand, if \mathbf{p} is in light shadow, then some light virtual obstacle is in place to intersect the direct path.

Specifically, we first partition the target ground area into M grid cells. A common partition approach is to use the uniform square grid with appropriate spacing according to the resolution requirement and the amount of measurement data. Then, a virtual obstacle map can be represented by an $M \times K$ matrix \mathbf{H} , where the k th column \mathbf{h}_k of \mathbf{H} represents the height of class- k virtual obstacle, and the m th entry of \mathbf{h}_k represents the height of the virtual obstacle

located at the m th grid cell. With such a notation, the likelihood $S_k(\mathbf{p}; \mathbf{H})$ of link \mathbf{p} belonging to propagation region \mathcal{D}_k can be constructed from the virtual obstacle map \mathbf{H} as follows.

1) *Propagation Regions with Hard Boundary*: It holds that $\sum_k S_k(\mathbf{p}; \mathbf{H}) = 1$ and $S_k(\mathbf{p}; \mathbf{H}) \in \{0, 1\}$, and constructed based on the following rule:

- $\mathbf{p} \in \mathcal{D}_0$, i.e., $S_0(\mathbf{p}; \mathbf{H}) = 1$, if there is no obstacle that intersects with the direct path between \mathbf{p}_u and \mathbf{p}_d .
- $\mathbf{p} \in \mathcal{D}_k$, i.e., $S_k(\mathbf{p}; \mathbf{H}) = 1$ for some $k \geq 1$, if a class- k obstacle intersects with the direct path between \mathbf{p}_u and \mathbf{p}_d , while no class- l , $l > k$, obstacle intersecting with the direct path.

Mathematically, denote $\mathcal{B}^{(i)}$ as the set of grid cells that are covered by the direct path between $\mathbf{p}_u^{(i)}$ and $\mathbf{p}_d^{(i)}$. In other words, if one projects the path $(\mathbf{p}_u^{(i)}, \mathbf{p}_d^{(i)})$ onto the ground, then the projected path passes through the grid cells and only the grid cells in $\mathcal{B}^{(i)}$. For each grid cell $m \in \mathcal{B}^{(i)}$, denote $z_m^{(i)}$ as the altitude when the path $(\mathbf{p}_u^{(i)}, \mathbf{p}_d^{(i)})$ passes over the grid cell.

It follows from the first rule above that $\mathbf{p}^{(i)} \in \mathcal{D}_0$ if $h_{m,k} < z_m^{(i)}$ for all $m \in \mathcal{B}^{(i)}$ and all $0 < k \leq K$, i.e., for all the relevant grid locations $m \in \mathcal{B}^{(i)}$, all classes of obstacles are below the corresponding critical altitude $z_m^{(i)}$; mathematically, $\mathbb{I}\{\mathbf{p}^{(i)} \in \mathcal{D}_0(\mathbf{H})\} = \mathbb{I}\{h_{m,l} < z_m^{(i)}, \forall m \in \mathcal{B}^{(i)}, \forall l > 0\}$. From the second rule above, if $\mathbf{p}^{(i)} \in \mathcal{D}_k$ for $k > 0$, we must have $h_{m,k} \geq z_m^{(i)}$ for some class- k obstacle at the m th grid cell, mathematically, $\mathbb{I}\{h_{m,k} \geq z_m^{(i)}, \exists m \in \mathcal{B}^{(i)}\} = 1$, and at the same time, we should also have $h_{m,l} < z_m^{(i)}$ for all $m \in \mathcal{B}^{(i)}$ and all $l \geq k + 1$, mathematically, $\mathbb{I}\{h_{m,l} < z_m^{(i)}, \forall m \in \mathcal{B}^{(i)}, \forall l > k\} = 1$. To summarize, it follows that

$$\mathbb{I}\{\mathbf{p}^{(i)} \in \mathcal{D}_k(\mathbf{H})\} = \begin{cases} \prod_{m \in \mathcal{B}^{(i)}} \prod_{l > 0} \mathbb{I}\{h_{m,l} < z_m^{(i)}\}, & \text{if } k = 0, \\ \left(1 - \prod_{m \in \mathcal{B}^{(i)}} (1 - \mathbb{I}\{h_{m,k} \geq z_m^{(i)}\})\right) \\ \quad \times \prod_{m \in \mathcal{B}^{(i)}} \prod_{l > k} \mathbb{I}\{h_{m,l} < z_m^{(i)}\}, & \text{if } k \geq 1. \end{cases} \quad (3)$$

Using the propagation regions defined in (3), the likelihood function $S_k(\mathbf{p}; \mathbf{H})$ in (1) can be chosen as $S_k(\mathbf{p}; \mathbf{H}) \triangleq \mathbb{I}\{\mathbf{p} \in \mathcal{D}_k(\mathbf{H})\}$.

2) *Propagation Regions with Soft Boundary*: To allow the likelihood $S_k(\mathbf{p}; \mathbf{H})$ to take fractional numbers in $[0, 1]$, we extend the hard boundary model by applying a spatial low-pass filter on the propagation regions \mathcal{D}_k defined in (3). Specifically, given a link \mathbf{p} , we evaluate a set of neighbor positions with offset ϵ_j from \mathbf{p} . By averaging $\mathbb{I}\{\mathbf{p} + \epsilon_j \in \mathcal{D}_k(\mathbf{H})\}$ with

weights ω_j , one can obtain the likelihood $S_k(\mathbf{p}; \mathbf{H})$. A common choice of filter coefficients ω_j can be obtained as a function of the distance $\|\epsilon_j\|_2$ from \mathbf{p} . In this paper, we consider a spatial filter that consists of a set of J uniform grid points $\epsilon_j, j = 0, 1, \dots, J - 1$, in 6D space centered at the origin with ϵ_0 chosen as $\epsilon_0 = \mathbf{0}$, and the weights are chosen as $\omega_j = c \cdot \exp(-\|\epsilon_j\|_2^2 / \sigma_\omega^2)$, where σ_ω is a parameter, and c is a normalization factor such that $\sum_{j=0}^{J-1} \omega_j = 1$.¹ Thus, the likelihood function $S_k(\mathbf{p}; \mathbf{H})$ parameterized by the virtual obstacle map \mathbf{H} is defined as

$$S_k(\mathbf{p}; \mathbf{H}) = \sum_{j=0}^{J-1} \omega_j \mathbb{I}\{\mathbf{p} + \epsilon_j \in \mathcal{D}_k(\mathbf{H})\} \quad (4)$$

which satisfies $\sum_{k=0}^K S_k(\mathbf{p}; \mathbf{H}) = 1$.

III. RADIO MAP CONSTRUCTION VIA ENVIRONMENT MAPPING

In this section, we jointly estimate the propagation parameter $\boldsymbol{\theta}$ and the virtual obstacle map \mathbf{H} for constructing the deterministic radio map $\bar{g}(\mathbf{p}; \boldsymbol{\theta}, \mathbf{H})$ in (2).

A. Formulation of the Radio Map Learning Problem

Consider taking measurements at transmit and receive location pairs $\{\mathbf{p}^{(i)}\}$ and recall $\mathbf{p} = (\mathbf{p}_u, \mathbf{p}_d)$. Based on (1), the measured RSS can be written as

$$y^{(i)} = \bar{g}(\mathbf{p}^{(i)}; \boldsymbol{\theta}, \mathbf{H}) + n^{(i)} \quad (5)$$

where $n^{(i)} = \xi(\mathbf{p}^{(i)}) + \tilde{n}^{(i)}$ captures both the random component $\xi(\mathbf{p})$ in (1) for the residual shadowing and the measurement noise $\tilde{n}^{(i)}$ which is assumed as independent and identically distributed with zero mean, variance σ_n^2 , and finite fourth-order moment.

The goal of this section is to estimate parameters $\boldsymbol{\theta}$ and \mathbf{H} from the set of noisy measurement data $\{(\mathbf{p}^{(i)}, y^{(i)})\}_{i=1}^N$ obtained from (5). A least-squares problem can be formulated as follows

$$\underset{\boldsymbol{\theta}, \mathbf{H} \succeq \mathbf{0}}{\text{minimize}} \quad f(\boldsymbol{\theta}, \mathbf{H}) \triangleq \frac{1}{N} \sum_{i=1}^N \left[y^{(i)} - \sum_{k=0}^K (\beta_k + \alpha_k d(\mathbf{p}^{(i)})) S_k(\mathbf{p}^{(i)}; \mathbf{H}) \right]^2 \quad (6)$$

where $d(\mathbf{p}^{(i)}) \triangleq \log_{10} \|\mathbf{p}_u^{(i)} - \mathbf{p}_d^{(i)}\|_2$ is the log-distance between $\mathbf{p}_u^{(i)}$ and $\mathbf{p}_d^{(i)}$ for the i th measurement.

Note that the least-squares problem (6) is difficult to solve using a standard solver. This is because the problem is *non-convex* in the joint variable $(\boldsymbol{\theta}, \mathbf{H})$ and the objective function

¹In general, the weights can be designed using a kernel function, where the smaller $\|\epsilon_j\|_2$, the larger the weight. The choice of the kernel and its parameters can be determined using a cross-validation approach.

$f(\boldsymbol{\theta}, \mathbf{H})$ is *discontinuous* due to the indicator functions used in (2)–(4). To circumvent these difficulties, we will exploit the property discovered in $f(\boldsymbol{\theta}, \mathbf{H})$.

B. Asymptotic Consistency of Radio Maps

Since the objective function $f(\boldsymbol{\theta}, \mathbf{H})$ in (6) contains randomness due to the measurement noise, we first find a *deterministic proxy* for $f(\boldsymbol{\theta}, \mathbf{H})$ under large N . Denote $\boldsymbol{\theta}^*$ and \mathbf{H}^* as the true parameters in the measurement model (5) and consider the following deterministic proxy function

$$\bar{f}(\boldsymbol{\theta}, \mathbf{H}) \triangleq \frac{1}{N} \sum_{i=1}^N \left[\bar{g}(\mathbf{p}^{(i)}; \boldsymbol{\theta}, \mathbf{H}) - \bar{g}(\mathbf{p}^{(i)}; \boldsymbol{\theta}^*, \mathbf{H}^*) \right]^2 \quad (7)$$

and it is clear that $\bar{f}(\boldsymbol{\theta}^*, \mathbf{H}^*) = 0$.

Lemma 1 (Deterministic Equivalence). *Suppose that the random component $\xi(\mathbf{p}^{(i)})$ in the measurement model (5) is weakly dependent, i.e., the covariance satisfies $\text{cov}(\xi(\mathbf{p}^{(i)}), \xi(\mathbf{p}^{(j)})) \rightarrow 0$, as $|i - j| \rightarrow \infty$ and $N \rightarrow \infty$, and moreover, the limit $\lim_{N \rightarrow \infty} \frac{1}{N} \sum_{i=1}^N \xi(\mathbf{p}^{(i)})^2$ exists and is finite.² Then, there exists a finite constant $0 < C < \infty$, such that*

$$f(\boldsymbol{\theta}, \mathbf{H}) \rightarrow \bar{f}(\boldsymbol{\theta}, \mathbf{H}) + C$$

in probability, for every $(\boldsymbol{\theta}, \mathbf{H})$, as $N \rightarrow \infty$.

Proof. See Appendix A. □

It follows from the above lemma that the parameters $(\boldsymbol{\theta}, \mathbf{H})$ that minimize the deterministic proxy $\bar{f}(\boldsymbol{\theta}, \mathbf{H})$ also minimize the least-squares cost $f(\boldsymbol{\theta}, \mathbf{H})$ asymptotically. As a result, analyzing the property of the deterministic proxy $\bar{f}(\boldsymbol{\theta}, \mathbf{H})$ may inspire efficient algorithms to solve (6) under large N .

It is also observed that there could be multiple local minima for both $f(\boldsymbol{\theta}, \mathbf{H})$ and $\bar{f}(\boldsymbol{\theta}, \mathbf{H})$. Specifically, the globally optimal solution $(\hat{\boldsymbol{\theta}}, \hat{\mathbf{H}})$ to the least-squares problem (6) may differ from the true parameter $(\boldsymbol{\theta}^*, \mathbf{H}^*)$ even at the asymptotic regime. Yet, we are not interested in the estimated parameters $(\hat{\boldsymbol{\theta}}, \hat{\mathbf{H}})$, but the radio map $\bar{g}(\mathbf{p}; \hat{\boldsymbol{\theta}}, \hat{\mathbf{H}})$ constructed from these parameters. In other words, the focus is not on reconstructing the actual buildings or identifying the true parameters $(\boldsymbol{\theta}^*, \mathbf{H}^*)$, but to extract consistent environment semantics for constructing radio maps.

²If the process $\xi(\mathbf{p})$ is segment-wise second-order stationary within each propagation segment, then the limit exists if one samples each propagation segment with a fixed probability, for example, under uniform sampling over the entire area.

The following corollary shows that one may obtain *asymptotically consistent* radio maps even the globally optimal solution $(\hat{\boldsymbol{\theta}}, \hat{\mathbf{H}})$ differs from the true parameter $(\boldsymbol{\theta}^*, \mathbf{H}^*)$; here, consistency means that radio maps are identical $\bar{g}(\mathbf{p}^{(i)}; \hat{\boldsymbol{\theta}}, \hat{\mathbf{H}}) = \bar{g}(\mathbf{p}^{(i)}; \boldsymbol{\theta}^*, \mathbf{H}^*)$ at the measurement locations $\{\mathbf{p}^{(i)}\}$.

Corollary 1 (Asymptotic Consistency of Radio Maps). *It holds that, as $N \rightarrow \infty$,*

$$\bar{f}(\hat{\boldsymbol{\theta}}, \hat{\mathbf{H}}) = \frac{1}{N} \sum_{i=1}^N \left(\bar{g}(\mathbf{p}^{(i)}; \hat{\boldsymbol{\theta}}, \hat{\mathbf{H}}) - \bar{g}(\mathbf{p}^{(i)}; \boldsymbol{\theta}^*, \mathbf{H}^*) \right)^2 \rightarrow 0$$

where $(\hat{\boldsymbol{\theta}}, \hat{\mathbf{H}})$ is the globally optimal solution to (6).

Proof. By definition, the minimum value of $\bar{f}(\boldsymbol{\theta}, \mathbf{H})$ is obtained as $\bar{f}(\boldsymbol{\theta}^*, \mathbf{H}^*) = 0$, and therefore, $\bar{f}(\boldsymbol{\theta}, \mathbf{H}) + C$ can be globally minimized to C . Since $f(\boldsymbol{\theta}, \mathbf{H}) \rightarrow \bar{f}(\boldsymbol{\theta}, \mathbf{H}) + C$ from Lemma 1, $f(\boldsymbol{\theta}, \mathbf{H})$ is also asymptotically and globally minimized to $f(\hat{\boldsymbol{\theta}}, \hat{\mathbf{H}}) \rightarrow C$, which implies that $\bar{f}(\hat{\boldsymbol{\theta}}, \hat{\mathbf{H}}) \rightarrow 0$ as $N \rightarrow \infty$. \square

C. Solution to the Propagation Parameter $\boldsymbol{\theta}$

It can be easily verified that given the variable \mathbf{H} , the problem (6) is convex in $\boldsymbol{\theta}$. To see this, denote $\mathbf{X} \in \mathbb{R}^{N \times (2K+2)}$ as log-distance data matrix, where the even elements in the i th row of \mathbf{X} equal to $d(\mathbf{p}^{(i)})$ and the odd elements in the i th row of \mathbf{X} equal to 1. Arrange the elements in the variable $\boldsymbol{\theta} \in \mathbb{R}^{2K+2}$ as $\boldsymbol{\theta} = [\alpha_0 \ \beta_0 \ \alpha_1 \ \beta_1 \ \cdots \ \alpha_K \ \beta_K]^T$ as the path loss parameter vector for the sub-models. Stack the measurement value $y^{(i)}$ into a vector $\mathbf{y} = [y^{(1)} \ y^{(2)} \ \cdots \ y^{(N)}]^T \in \mathbb{R}^N$. Finally, denote $\mathbf{S} \in \mathbb{R}^{N \times (2K+2)}$ as the likelihood matrix, where $[\mathbf{S}]_{i,2k} = [\mathbf{S}]_{i,2k+1} = S_k(\mathbf{p}^{(i)}; \mathbf{H})$. Then, for a fixed \mathbf{H} , problem (6) can be written as

$$\underset{\boldsymbol{\theta}}{\text{minimize}} \quad \|(\mathbf{S} \circ \mathbf{X})\boldsymbol{\theta} - \mathbf{y}\|_2^2 \quad (8)$$

where \circ is the Hadamard product, *i.e.*, $[\mathbf{S} \circ \mathbf{X}]_{ij} = [\mathbf{S}]_{ij}[\mathbf{X}]_{ij}$. Problem (8) is unconstrained quadratic programming, and it is convex with respect to (w.r.t.) $\boldsymbol{\theta}$. It can be solved by setting the derivative to zero, and the solution is given by

$$\hat{\boldsymbol{\theta}} = ((\mathbf{S} \circ \mathbf{X})^T (\mathbf{S} \circ \mathbf{X}))^{-1} (\mathbf{S} \circ \mathbf{X})^T \mathbf{y}. \quad (9)$$

Proposition 1. *Under \mathbf{H}^* , the solution in (9) is an unbiased estimator of $\boldsymbol{\theta}^*$, *i.e.*, $\mathbb{E}\{\hat{\boldsymbol{\theta}}\} = \boldsymbol{\theta}^*$.*

Proof. With \mathbf{H}^* , the observation model can be written as $\mathbf{y} = (\mathbf{S}^* \circ \mathbf{X})\boldsymbol{\theta} + \mathbf{n}$, where \mathbf{n} is a vector stacking n . Therefore, it is a standard least-squares estimation problem for a linear observation model \mathbf{y} with zero mean noise \mathbf{n} . It is well-known that the least-squares estimator (9) in this case is unbiased [29]. \square

D. Quasiconvexity in the Environment Parameter \mathbf{H}

While problem (6) is convex in $\boldsymbol{\theta}$ by fixing \mathbf{H} , it is still non-convex in \mathbf{H} by fixing $\boldsymbol{\theta}$. However, we discover that \mathbf{H} is partially quasiconvex, which can be later exploited for efficient algorithm design.

First, consider the $K = 1$ case, where there are two propagation regions, LOS and NLOS, and the matrix \mathbf{H} degenerates to a column vector \mathbf{h} .

Theorem 1 (Quasiconvexity for $K = 1$ under Soft Boundary). *Suppose that the filter coefficient ω_0 in (4) satisfies $\omega_0 \geq \frac{2}{3}$. Given a vector $\mathbf{h}' \succeq \mathbf{h}^*$ and an index m , consider the interval $\mathcal{I}_m \triangleq \{\mathbf{h} \in \mathbb{R}^M : 0 \leq h_m \leq H_{max}, h_j = h'_j, \forall j \neq m\}$. Then, $\bar{f}(\boldsymbol{\theta}^*, \mathbf{h})$ in (7) is quasiconvex over the interval \mathcal{I}_m .*

Proof. See Appendix B. □

The above result implies that given a variable $\mathbf{h} \succeq \mathbf{h}^*$, the function $\bar{f}(\boldsymbol{\theta}^*, \mathbf{h})$ is partially quasiconvex w.r.t. to each entry h_m with all the other entries $h_j, j \neq m$, fixed. As a result of the partial quasiconvexity, there exists \hat{h}_m , such that, for $h_m < \hat{h}_m$, \bar{f} is non-increasing in h_m , and for $h_m > \hat{h}_m$, \bar{f} is non-decreasing.

Next, consider the case of a general K and the propagation regions being modeled with hard boundaries, *i.e.*, the likelihood function is chosen as $S_k(\mathbf{p}; \mathbf{H}) = \mathbb{I}\{\mathbf{p} \in \mathcal{D}_k(\mathbf{H})\}$ as in (3). The following result shows that the partial quasiconvexity in Theorem 1 also holds.

Theorem 2 (Quasiconvexity under Hard Boundary). *Given a matrix $\mathbf{H}' \succeq \mathbf{H}^*$ and an index (m, k) , define the interval $\mathcal{I}_{m,k} \triangleq \{\mathbf{H} \in \mathbb{R}^{M \times K} : 0 \leq h_{m,k} \leq H_{max}, h_{j,l} = h'_{j,l}, \forall (j, l) \neq (m, k)\}$. Then, $\bar{f}(\boldsymbol{\theta}^*, \mathbf{H})$ is quasiconvex over the interval $\mathcal{I}_{m,k}$.*

Proof. See Appendix C. □

Theorems 1 and 2 imply that if we focus on each individual entry $h_{m,k}$ in the variable \mathbf{H} , then $\bar{f}(\boldsymbol{\theta}, \mathbf{H})$ first decreases and then increases. More specifically, according to the fact that $\bar{f}(\boldsymbol{\theta}, \mathbf{H})$ in (7) is constructed from a number of indicator functions in (3) and (4), $\bar{f}(\boldsymbol{\theta}, \mathbf{H})$ appears like a *staircase* function that first steps down along the interval $\mathcal{I}_{m,k}$, reaching the bottom around $h_{m,k}^*$, and then steps up, where the bottom appears as a flat *basin* as shown in Fig. 2.

To characterize the basin of \bar{f} over $\mathcal{I}_{m,k}$, define a function

$$\bar{f}_{m,k}(h_{m,k}; \boldsymbol{\theta}, \mathbf{H}_{m,k}^-) = \bar{f}(\boldsymbol{\theta}, \mathbf{H}) \quad (10)$$

of the scalar variable $h_{m,k}$ with the other variables $\boldsymbol{\theta}$ and $\mathbf{H}_{m,k}^-$ held fixed, where $\mathbf{H}_{m,k}^- = \{h_{j,l} : \forall (j,l) \neq (m,k)\}$ is a collection of entries from the matrix \mathbf{H} except the (m,k) th one. The basin is defined as the interval $\mathcal{I}_{m,k}(\boldsymbol{\theta}, \mathbf{H}) \triangleq \{z : \bar{f}_{m,k}(z; \boldsymbol{\theta}, \mathbf{H}_{m,k}^-) \leq \bar{f}_{m,k}(h; \boldsymbol{\theta}, \mathbf{H}_{m,k}^-), \forall 0 \leq h \leq H_{\max}\}$. We are interested in the largest value in the basin

$$\hat{h}_{m,k}(\boldsymbol{\theta}, \mathbf{H}) \triangleq \sup\{\mathcal{I}_{m,k}(\boldsymbol{\theta}, \mathbf{H})\} \quad (11)$$

where the algorithm to solve (11) will be developed in Section III-E. With the notation of $\hat{h}_{m,k}(\boldsymbol{\theta}, \mathbf{H})$, the following property can be established.

Theorem 3 (Consistency). *Suppose $\mathbf{H} \succeq \mathbf{H}^*$ and consider the interval $\mathcal{I}_{m,k}$ as defined in Theorem 2. Then, $\hat{h}_{m,k}(\boldsymbol{\theta}^*, \mathbf{H}) \geq h_{m,k}^*$. Moreover, given $\mathbf{H}'' \succeq \mathbf{H}' \succeq \mathbf{H}^*$, it holds that $\hat{h}_{m,k}(\boldsymbol{\theta}^*, \mathbf{H}'') \geq \hat{h}_{m,k}(\boldsymbol{\theta}^*, \mathbf{H}') \geq h_{m,k}^*$.*

Proof. See Appendix D. □

As inspired from Theorems 1–3, when $\boldsymbol{\theta}$ is sufficiently close to $\boldsymbol{\theta}^*$, an efficient algorithm to optimize \mathbf{H} can proceed as follows. First, set the initial value of \mathbf{H} as $h_{m,k} = H_{\max}$ for all m, k . Then, for each element $h_{m,k}$, find $\hat{h}_{m,k}$ that minimizes $\bar{f}(\boldsymbol{\theta}, \mathbf{H})$, and repeat this step until convergence. This approach is summarized in Algorithm 1 and its convergence can be analyzed as follows.

Let $\mathbf{H}(t)$ denotes the variable \mathbf{H} at the t th iteration. Theorem 3 implies the convergence of $h_{m,k}(t)$ for $\boldsymbol{\theta} = \boldsymbol{\theta}^*$. Suppose at $t > 1$, given that $\mathbf{H}(t-1) \succeq \mathbf{H}(t) \succeq \mathbf{H}^*$, Theorem 3 implies that $\hat{h}_{m,k}(t-1) \geq \hat{h}_{m,k}(t) \geq h_{m,k}^*$, $\forall m, k$, under $\boldsymbol{\theta}^*$, and consequently, $\mathbf{H}(t) \succeq \mathbf{H}(t+1) \succeq \mathbf{H}^*$. As $t = 1$ can be checked to satisfy $\hat{h}_{m,k}(1) \geq \hat{h}_{m,k}(2) \geq h_{m,k}^*$ due to the initialization, by induction, $\hat{h}_{m,k}(t) \geq \hat{h}_{m,k}(t+1) \geq h_{m,k}^*$ is satisfied for all t , which means that Algorithm 1 constructs monotonically decreasing and lower bounded sequences $h_{m,k}(t)$, which implies the convergence of $\mathbf{H}(t)$.

As a side note, finding $\boldsymbol{\theta}^*$ is relatively easier as suggested by a lot of numerical experiments. The intuition is that $\boldsymbol{\theta}^*$ has just $2K + 2$ variables, and thus, depends on global statistics, not very sensitive to \mathbf{H} under large N .

E. Optimizing \mathbf{H} via Local Polynomial Approximation

The remaining challenge is to compute $\hat{h}_{m,k}(\boldsymbol{\theta}, \mathbf{H})$ in (11). A common approach finding the minimizer of a quasiconvex function over a bounded interval is to perform a bisection search for the critical point. However, as discussed after Theorem 2, the function $\bar{f}(\boldsymbol{\theta}, \mathbf{H})$ appears as a staircase in each variable $h_{m,k}$, where the derivative is zero almost everywhere,

Algorithm 1 Learning the deterministic component $\bar{g}(\mathbf{p})$

- 1) Initialize $\mathbf{H}(1) = \mathbf{1}H_{\max}$, $\boldsymbol{\theta}(1)$ using expectation-maximization (EM) in [26], and iteration $t = 1$.
 - 2) Optimize \mathbf{H} : For each (m, k) , update $h_{m,k}(t+1) = \hat{h}_{m,k}$ as defined in (11) based on $\boldsymbol{\theta}(t)$ and $\mathbf{H}_{m,k}^-(t)$. Specifically, the following bisection search is used:
 - a) Initialize $h_{\min} = 0$ and $h_{\max} = H_{\max}$.
 - b) Set $h_{m,k} = \frac{1}{2}(h_{\min} + h_{\max})$ and find the minimizer a_1^* of (12).
 - c) If $a_1^* < 0$, then $h_{\min} \leftarrow h_{m,k}$; if $a_1^* > 0$, then $h_{\max} \leftarrow h_{m,k}$.
 - d) Repeat from Step 2b until $|h_{\max} - h_{\min}| < \epsilon$, for which output $\hat{h}_{m,k} = h_{\max}$.
 - 3) Optimize $\boldsymbol{\theta}$: Update $\boldsymbol{\theta}(t+1) = \hat{\boldsymbol{\theta}}$ based on $\mathbf{H}(t+1)$ according to (9). Set $t \leftarrow t+1$ and repeat from Step 2 until $\frac{1}{MK} \|\mathbf{H}(t+1) - \mathbf{H}(t)\|_F < \epsilon_0$.
-

as illustrated in Fig. 2. Moreover, the staircase function $\bar{f}(\boldsymbol{\theta}, \mathbf{H})$ is not available, but only its noisy counterpart $f(\boldsymbol{\theta}, \mathbf{H})$ in (6) is accessible to the algorithm.

We propose to smooth $f(\boldsymbol{\theta}, \mathbf{H})$ without losing the partial quasiconvex property of $\bar{f}(\boldsymbol{\theta}, \mathbf{H})$. One possibility is to employ local polynomial approximation to estimate $\bar{f}(\boldsymbol{\theta}, \mathbf{H})$ from $f(\boldsymbol{\theta}, \mathbf{H})$. Specifically, we use a polynomial to approximate $\bar{f}_{m,k}(h; \boldsymbol{\theta}, \mathbf{H}_{m,k}^-)$ in (10) at the neighborhood of $h_{m,k}$:

$$\tilde{f}_{m,k}(h; \boldsymbol{\alpha}, h_{m,k}) = a_0 + a_1(h - h_{m,k}) + a_2(h - h_{m,k})^2 + \dots$$

where the coefficients $\boldsymbol{\alpha} = (a_0, a_1, \dots)$ are computed by sampling $f_{m,k}(h; \boldsymbol{\theta}, \mathbf{H}_{m,k}^-)$ over a set \mathcal{Z} of scattered points z in the interval $[0, H_{\max}]$ and minimizing the weighted squared error:

$$\sum_{z \in \mathcal{Z}} \left(f_{m,k}(z; \boldsymbol{\theta}, \mathbf{H}_{m,k}^-) - \tilde{f}_{m,k}(z; \boldsymbol{\alpha}, h_{m,k}) \right)^2 K_b(z - h_{m,k}). \quad (12)$$

Here, $f_{m,k}(h; \boldsymbol{\theta}, \mathbf{H}_{m,k}^-)$ is a notation defined according to $f(\boldsymbol{\theta}, \mathbf{H})$ in a way similar to the definition of $\bar{f}_{m,k}(h; \boldsymbol{\theta}, \mathbf{H}_{m,k}^-)$ in (10), and is computed via (6). The term $K_b(u)$ is a kernel function that assigns a high weight if the distance $u = |z - h_{m,k}|$ is small, and a low weight if the distance u is large. It was found that the Epanechnikov kernel $K_b(u) = \frac{3}{4b} \left(1 - \left(\frac{u}{b}\right)^2\right)_+$ minimizes the asymptotic approximation error of the polynomial $\tilde{f}_{m,k}(h; \boldsymbol{\alpha}, h_{m,k})$ for a given window size b [30]. Here, we can adapt b according to the volume of the measurement data such that $\tilde{f}_{m,k}$ is smoothed and the gradient is non-degenerated.

It is clear that $a_1^*(h_{m,k})$, from the minimizer of (12), is the approximated (but non-degenerated) gradient of \bar{f} at $h = h_{m,k}$. Note that it suffices to determine the sign of

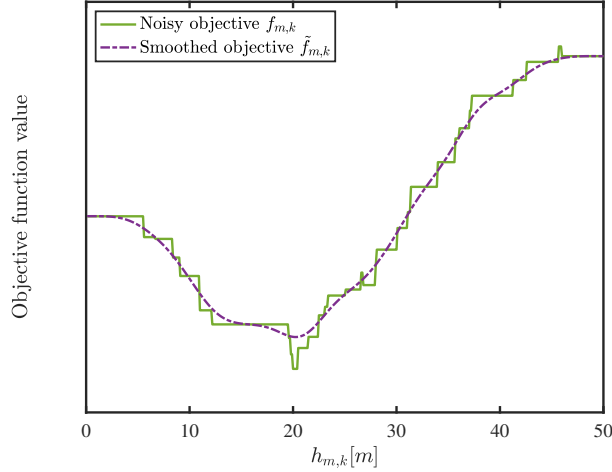


Figure 2. Illustration of $f_{m,k}$ (solid line) and the smoothed one using local polynomial approximation (dashed line).

$a_1^*(h_{m,k})$ due to the quasiconvexity in Theorems 1 and 2. Specifically, we can perform a bisection search to seek the minimizer $\hat{h}_{m,k}$ in (11) as follows: (i) Initialize $h_{\min} = 0$ and $h_{\max} = H_{\max}$. (ii) Set $h_{m,k} = \frac{1}{2}(h_{\min} + h_{\max})$ and find the minimizer a_1^* from minimizing (12). (iii) If $a_1^* < 0$, then $h_{\min} \leftarrow h_{m,k}$; if $a_1^* > 0$, then $h_{\max} \leftarrow h_{m,k}$. (iv) Repeat from Step (ii) until $|h_{\max} - h_{\min}| < \epsilon$, and output $\hat{h}_{m,k} = h_{\max}$.

F. The Overall Algorithm

One can employ alternative optimization to repeatedly optimize $\boldsymbol{\theta}$ according to (9) and \mathbf{H} according to (11) to search for the jointly optimal solution $(\hat{\boldsymbol{\theta}}, \hat{\mathbf{H}})$ as summarized in Algorithm 1. The deterministic radio map is constructed as

$$\hat{g}(\mathbf{p}) \triangleq \bar{g}(\mathbf{p}; \hat{\boldsymbol{\theta}}, \hat{\mathbf{H}}).$$

IV. RECONSTRUCTING THE SHADOWING USING KRIGING

After reconstructing the deterministic radio map $\hat{g}(\mathbf{p})$ from Section III, this section focuses on constructing the residual shadowing map $\xi(\mathbf{p})$ for the radio map model (1).

Denote $\hat{\xi}^{(i)} = y^{(i)} - \hat{g}(\mathbf{p}^{(i)})$ as the estimated shadowing at $\mathbf{p}^{(i)}$. The goal is to interpolate the random process $\xi(\mathbf{p})$ based on $\hat{\xi}^{(i)}$ constructed at various locations $\mathbf{p}^{(i)}$ using the a data-driven approach.

Recall the measurement model $y^{(i)}$ in (5) and the noise model $n = \xi(\mathbf{p}^{(i)}) + \tilde{n}$, we obtain

$$\begin{aligned}\hat{\xi}^{(i)} &= \bar{g}(\mathbf{p}^{(i)}; \boldsymbol{\theta}^*, \mathbf{H}^*) + \xi(\mathbf{p}^{(i)}) + \tilde{n} - \hat{g}(\mathbf{p}^{(i)}) \\ &= \xi(\mathbf{p}^{(i)}) + \tilde{n} + (\bar{g}(\mathbf{p}^{(i)}; \boldsymbol{\theta}^*, \mathbf{H}^*) - \hat{g}(\mathbf{p}^{(i)})) \\ &\approx \xi(\mathbf{p}^{(i)}) + \tilde{n}\end{aligned}\tag{13}$$

where the approximation is asymptotically accurate because the term $\bar{g}(\mathbf{p}^{(i)}; \boldsymbol{\theta}^*, \mathbf{H}^*) - \hat{g}(\mathbf{p}^{(i)})$ tends to 0 as $N \rightarrow \infty$ according to Corollary 1.

Consider constructing $\hat{\xi}(\mathbf{p})$ at $\mathbf{p} \notin \{\mathbf{p}^{(i)}\}$ as a linear combination of the measurements $\xi(\mathbf{p}^{(i)})$

$$\hat{\xi}(\mathbf{p}) = \sum_{i=1}^N \lambda_i(\mathbf{p}) \xi(\mathbf{p}^{(i)})\tag{14}$$

where the set of coefficients $\{\lambda_i(\mathbf{p})\}$ depends on location \mathbf{p} .

For a given location \mathbf{p} , a widely used Kriging approach [15], [16] determines the coefficients $\lambda_i \triangleq \lambda_i(\mathbf{p})$ by minimizing the variance of the estimation error

$$\underset{\mathbf{1}^T \boldsymbol{\lambda} = 1}{\text{minimize}} \quad \mathbb{V} \left\{ \hat{\xi}(\mathbf{p}) - \xi(\mathbf{p}) \right\}.\tag{15}$$

Substituting (13) and (14) into (15), the objective function becomes

$$\begin{aligned}\mathbb{V} \left\{ \hat{\xi}(\mathbf{p}) - \xi(\mathbf{p}) \right\} &= \mathbb{V} \left\{ \sum_{i=1}^N \lambda_i(\mathbf{p}) \xi(\mathbf{p}^{(i)}) - \xi(\mathbf{p}) \right\} \\ &= \mathbb{V} \left\{ \sum_{i=1}^N \lambda_i \hat{\xi}^{(i)} - \xi(\mathbf{p}) \right\} - \sum_{i=1}^N \lambda_i^2 \mathbb{V} \{ \tilde{n} \}\end{aligned}$$

where the derivation is due to the fact that the measurement noise \tilde{n} is independent of the residual shadowing process $\xi(\mathbf{p})$.

To compute the variance above, we need to build a *semivariogram* as follows.

A. Semivariogram

Under the stationary assumption on the process $\xi(\mathbf{p})$, the *semivariogram* for $\xi(\mathbf{p})$ is defined as a function $v(\|\mathbf{u}\|_2) = \frac{1}{2} \mathbb{E} \{ (\xi(\mathbf{p} + \mathbf{u}) - \xi(\mathbf{p}))^2 \}$. However, the function $v(u)$ is unavailable, one needs to learn the semivariogram model from the data. A commonly used one is the exponential semivariogram model:

$$\bar{v}(u; \boldsymbol{\alpha}) = \alpha_s^2 \left(1 - \exp\left(-\frac{u}{\alpha_r}\right) \right)\tag{16}$$

where the parameter $\boldsymbol{\alpha} = (\alpha_s, \alpha_r)$ can be obtained through a least-squares fitting from the data $\{\mathbf{p}^{(i)}, \hat{\xi}^{(i)}\}$. Specifically, the best model parameters can be obtained as the solution to the following least-squares problem:

$$\underset{\boldsymbol{\alpha}}{\text{minimize}} \quad \sum_{i,j} \left(\bar{v}(\|\mathbf{p}^{(i)} - \mathbf{p}^{(j)}\|_2; \boldsymbol{\alpha}) - [\hat{\xi}^{(i)} - \hat{\xi}^{(j)}]^2 \right)^2.$$

B. Constructing the Residual Shadowing using Kriging

To solve (15), we can use the Lagrange multiplier and the Lagrange function is

$$\begin{aligned} L(\boldsymbol{\lambda}, \mu) &= \mathbb{V} \left\{ \hat{\xi}(\mathbf{p}) - \xi(\mathbf{p}) \right\} + \mu \left(\sum_{i=1}^N \lambda_i - 1 \right) \\ &= \mathbb{E} \left\{ \left(\sum_{i=1}^N \lambda_i \hat{\xi}^{(i)} - \xi(\mathbf{p}) \right)^2 \right\} - \sum_{i=1}^N \lambda_i^2 \sigma_n^2 + \mu \left(\sum_{i=1}^N \lambda_i - 1 \right) \\ &= \sum_{i=1}^N \lambda_i \mathbb{E} \left\{ \left(\hat{\xi}^{(i)} - \xi(\mathbf{p}) \right)^2 \right\} - \frac{1}{2} \sum_{i,j} \lambda_i \lambda_j \mathbb{E} \left\{ \left(\hat{\xi}^{(i)} - \hat{\xi}^{(j)} \right)^2 \right\} - \sum_{i=1}^N \lambda_i^2 \sigma_n^2 + \mu \left(\sum_{i=1}^N \lambda_i - 1 \right) \end{aligned}$$

where $\mathbb{E} \left\{ \left(\hat{\xi}^{(i)} - \xi(\mathbf{p}) \right)^2 \right\}$ and $\mathbb{E} \left\{ \left(\hat{\xi}^{(i)} - \hat{\xi}^{(j)} \right)^2 \right\}$ can be calculated by (16). Then, take the partial derivatives of $L(\boldsymbol{\lambda}, \mu)$ and set them to zero [16]. We will get $\boldsymbol{\lambda}$ and use them in the estimator $\hat{\xi}(\mathbf{p}) = \sum_{i=1}^N \lambda_i \hat{\xi}^{(i)}$ for the shadowing component.

V. NUMERICAL RESULTS

We study a 310 meters by 340 meters area in central Shanghai, as illustrated in Fig. 5. There are dozens of buildings and other objects with heights ranging from 10 to 130 meters. Their shapes include cubes, columns, and some irregular shapes.³ We chose 100 user locations at random on the ground level, and 50,000 UAV locations uniformly at random from various altitudes. Based on the 3D city map and the deployment of the users and UAVs, two radio map datasets are generated:⁴

Dataset A: The radio map is simulated according to the radio map model $g(\mathbf{p})$ in (1) with $K = 1$ and path loss parameters $(\alpha_0, \beta_0) = (-22, -28)$ and $(\alpha_1, \beta_1) = (-36, -22)$. Independent and identically distributed (i.i.d.) Gaussian measurement noise with zero mean and standard deviation $\sigma_n \in \{3, 7\}$ dB is added to model the shadowing $\xi(\mathbf{p})$.

Dataset B: The radio map $g(\mathbf{p})$ is generated using Remcom Wireless Insite, a commercial 3D ray-tracing software. Up to 6 reflections and 1 diffraction are simulated, and other

³The 3D city map is available at <https://www.openstreetmap.org>.

⁴The code and dataset are available at <https://github.com/6wj/radiomap-uav>.

parameters are set as default. The material of all structures is considered to be concrete. The waveforms are chosen as narrowband sinusoidal signals at frequencies bands 2.5 GHz and 28 GHz, respectively, in different experiments.

The proposed method reconstructs a radio map with a virtual obstacle map of roughly $M = 1,200$ grid cells with 9 meter spacing between grid points. The choice of M is discussed later.

A. Radio Map Reconstruction

We first evaluate the performance of radio map reconstruction from Dataset A. The performance is evaluated in mean absolute error (MAE) $e = \mathbb{E}\{|\hat{g}(\mathbf{p}) - g(\mathbf{p})|\}$ for the reconstructed radio map.

To make a fair comparison, the following baseline schemes are evaluated:

- 1) KNN [13], [14]: To construct the channel quality at each 6D location \mathbf{p} , the algorithm first selects 5 measurement samples that are closest to \mathbf{p} from the training set $\{\mathbf{p}^{(i)}\}$ and form the neighbor set as $\mathcal{N}(\mathbf{p})$; then, the channel quality at \mathbf{p} is computed as $\hat{g}(\mathbf{p}) = \mu^{-1} \sum_{i \in \mathcal{N}(\mathbf{p})} w(\mathbf{p}, \mathbf{p}^{(i)}) y^{(i)}$, where $w(\mathbf{p}, \mathbf{p}^{(i)}) = \exp[-\|\mathbf{p} - \mathbf{p}^{(i)}\|_2^2 / (2s^2)]$ with a properly chosen parameter $s = 55$ meters and $\mu = \sum_{i \in \mathcal{N}(\mathbf{p})} w(\mathbf{p}, \mathbf{p}^{(i)})$ is a normalizing factor.
- 2) Kriging [16]: The radio map $\hat{g}(\mathbf{p})$ is constructed based on all the measurement samples $\{(\mathbf{p}^{(i)}, y^{(i)})\}$ using a similar model as in (14) and the model parameters are computed using the method in Section IV.

Several 2D slices of reconstructed radio maps are demonstrated in Fig. 3. It is observed that the LOS/NLOS structure in the radio maps can be roughly reconstructed.

The left one in Fig. 4 shows the MAE for the radio map reconstruction in terms of the number of training samples for Dataset A, where dashed lines for $\sigma_n = 3$ dB and solid lines for $\sigma_n = 7$ dB in standard deviation of the measurement noise. It is observed that the proposed radio map reconstruction method can reduce the MAE by 2–4 dB, corresponding to an order of reduction in the sampling complexity, *e.g.*, the proposed method requires only 500 samples to achieve a similar or lower MAE that is achieved by Kriging or KNN using 5,000 samples. In addition, the proposed method is shown to be robust to measurement noise, where a similar MAE is achieved under either 3 dB or 7 dB noise in standard deviation.

The right one in Fig. 4 shows the MAE versus the number of training samples from Dataset B. Two observations are made:

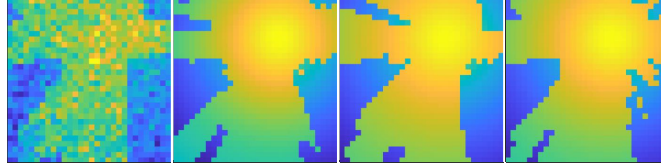


Figure 3. 2D slices of radio maps from a fixed user position and fixed UAV height, where each pixel represents the link quality between the UAV at the corresponding (x, y) position and the ground user at a fixed position. From left to right: the true radio map, and the deterministic radio maps $\bar{g}(\mathbf{p}; \hat{\boldsymbol{\theta}}, \hat{\mathbf{H}})$ reconstructed from 400, 900, 2500 measurement samples, respectively.

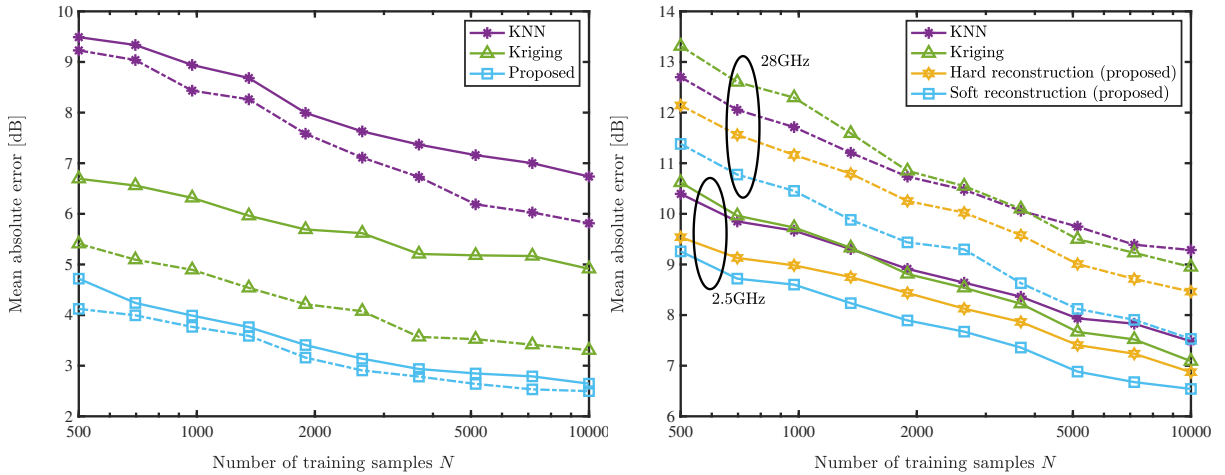


Figure 4. Left: reconstruction error versus the number of training samples N , where solid lines are from 7 dB data and dashed lines are from 3 dB data; right: reconstruction error versus the number of training samples N , where solid lines are from data of the frequency at 2.5 GHz and dashed lines are from 28 GHz data.

- Geometry-Awareness:** The proposed method, which estimates both the environment-aware deterministic radio map $\bar{g}(\mathbf{p})$ and the residual shadowing $\xi(\mathbf{p})$, can bring down the MAE by 1–2 dB, corresponding to more than 50% reduction in the required measurement samples. This confirms that recovering the virtual geometry of propagation environment with radio semantics does help radio map reconstruction.
- Spatial Correlation:** The proposed hard reconstruction scheme uses the indicator function in (3) to make a hard decision on the propagation condition, whereas, the proposed soft reconstruction scheme uses the likelihood function (4) for the propagation condition. Although the two methods have the same number of parameters to estimate in the learning phase, the soft reconstruction model (4) has a higher model complexity. Specifically, the link status depends on a lot more virtual map parameters $h_{m,k}$ in the soft reconstruction model (4), whereas, in the hard boundary model (3), the status

of the same link depends on only a subset of the parameters from that of the soft model (4); the hard model (3) is a special case of the soft one. As a result, given enough training data, the soft reconstruction model (4) requires a higher computational complexity in the reconstruction phase but achieves substantially better performance than hard reconstruction.

B. Reconstructing the Geometry of the Radio Environment

We demonstrate the recovered geometry of the surroundings that represent the propagation environment with radio semantics.

Fig. 5 shows the environment reconstruction under Dataset A and 7 dB measurement noise. The left figure in Fig. 5 shows the city map of a local area, and the right figure shows the reconstructed virtual obstacle map from the RSS measurements. It is observed that the geometry of the reconstructed radio environment is roughly consistent with the city map.

Note that the two maps have different physical meanings. The city map represents objects seen by visual light via reflection and scattering, whereas, the virtual obstacle map represents objects “seen” by radio signals via penetration, diffraction, reflection, and scattering, etc. The virtual obstacle map serves as a low dimensional (2D) geometry interpretation of the radio environment.

Furthermore, we obtain some insights from our experiments for the choice of the parameters K and M in constructing the virtual obstacle map.

- **Performance-Complexity Tradeoff:** The number of virtual obstacle types K and the number of grid cells M affect the model complexity as seen in Section II-B. Specifically, the number of parameters to be estimated (such as $h_{m,k}$ in (3)) scales as $\mathcal{O}(MK)$. In an ideal case, a larger model may provide a better approximation to reality. For example, at $K = 2$, the proposed model not only differentiates NLOS links from LOS ones, but also differentiates whether the NLOS links suffer from strong attenuation or light attenuation. However, a model with a larger K or M also requires more training data and costs a higher computational burden to estimate the model parameters.
- **Spatial Resolution and Measurement Data Requirement Tradeoff:** The parameters K and M also affect the spatial resolution of the reconstructed radio map. A larger M corresponds to a finer spacing of grid cells for estimating the virtual obstacles, and a larger K corresponds to more types of virtual obstacles per grid cell. Therefore, it is expected that a model with larger K and M may represent finer details in a radio map, and likewise, require more measurement data and more computational resources.

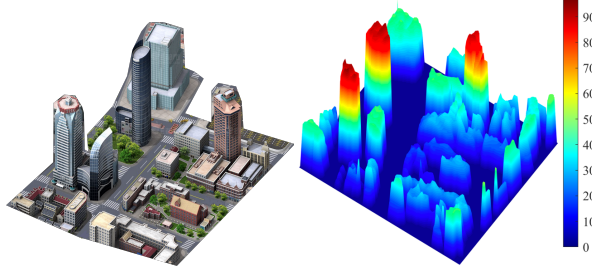


Figure 5. The left figure is the ground truth of $K = 1$ virtual obstacle model. The right figure demonstrates $K = 1$ virtual obstacle height estimation $\hat{\mathbf{H}}$. The color represents the heights in meters.

Our experiments suggest that the best practice for choosing M and K is such that there are on average 5–20 measurement links passing over a grid cell for each type of virtual obstacle. Moreover, our earlier work also studied a method to dynamically adjust the resolution M locally according to the amount of measurement data [28].

C. Application in UAV-aided Relay Communication

Consider a scenario of placing a UAV relay in 3D to establish a relay link for two ground users probably in deep shadow in a dense urban environment. For demonstration purpose, suppose that a half-duplex decode-and-forward relay strategy is used for a narrowband single antenna system. We evaluate the end-to-end capacity from one user to the other via the UAV relay. The capacity is clearly a function of the UAV position \mathbf{p}_d and the radio environment: $C_{\text{DF}}(\mathbf{p}_d) = \frac{1}{2}W \min \{ \log_2(1 + \kappa P_b g_{d,b}(\mathbf{p}_d)), \log_2(1 + \kappa P_r g_{u,d}(\mathbf{p}_d)) \}$, where $W = 100$ MHz is the bandwidth, $\kappa = 0.5$ is a discount factor to capture the modulation and coding loss, $P_b, P_r = 104$ dB is the ratio of the transmission power 20 dBm over the received noise power $N_0 W$ with $N_0 = -164$ dBm/Hz, and $g_{d,b}(\mathbf{p}_d), g_{u,d}(\mathbf{p}_d)$ are channel gain depending on the UAV position.

We propose to maximize the relay channel capacity by optimizing the UAV position \mathbf{p}_d using the radio map $\tilde{g}(\mathbf{p}) = \hat{g}(\mathbf{p}) + \hat{\xi}(\mathbf{p})$ constructed in this paper. To benchmark the performance, we also evaluate baselines that optimize the UAV position based on the radio map, or propagation model, constructed by the following schemes found in the recent literature:

- 1) Statistical Map [9], [10]: Define $p(\phi(\mathbf{p}))$ as the LOS probability of the user–UAV position pair $\mathbf{p} = (\mathbf{p}_u, \mathbf{p}_d)$ given the elevation angle $\phi(\mathbf{p})$ from the user to the UAV. Then, the channel gain $g_{d,b}(\mathbf{p}_d)$ or $g_{u,d}(\mathbf{p}_d)$ is estimated as $p(\phi(\mathbf{p}))G_0(\mathbf{p}) + (1 - p(\phi(\mathbf{p})))G_1(\mathbf{p})$, where $G_k(\mathbf{p}) = a_k + b_k \log_{10} \tilde{d}(\mathbf{p})$ with $\tilde{d}(\mathbf{p})$ being the propagation distance. The

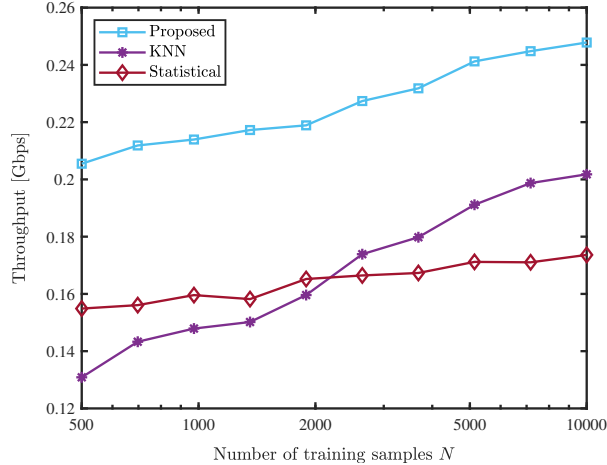


Figure 6. Average UAV-aided relay channel capacity evaluated over 1,225 user positions from Dataset B in a dense urban environment.

empirical distribution $p(\phi)$ is obtained via offline training based on data $\{(\mathbf{p}^{(i)}, y^{(i)})\}_{i=1}^N$, and the parameters a_k, b_k are empirically fitted from data under LOS (for $k = 0$) or under NLOS (for $k = 1$).

- 2) KNN-based Radio Map: The radio map is constructed using the KNN approach described in Section V-A.

Fig. 6 demonstrates the average capacity versus the number of training samples N from Dataset B for the 2.5 GHz case. Statistical method requires the least number of training samples before its performance saturates, because the model has the least parameters and a poor capability to describe the radio environment. The capacity of both the KNN-based approach and the proposed approach increases as the number of training samples N gets larger. The significant gain of the proposed scheme over the KNN-based approach can be understood from the fact that the proposed method reconstructs a radio map much more accurate than the KNN approach does. Specifically, the proposed scheme achieves more than 50% capacity gain over the KNN-based approach in the small sample regime (around 500 training samples); in addition, it also outperforms the statistical scheme by more than 30% capacity gain and the performance gain further increases when more training samples are used. Thus, we may conclude that an accurate radio map may substantially enhance the performance in a wireless communication system.

VI. CONCLUSION

This paper developed a radio map model and estimation algorithms for constructing radio maps from RSS measurements between aerial nodes and ground nodes. The core idea is

to construct a multi-class 3D virtual obstacle model from the RSS measurement data to capture the geometry of the environment with radio semantics. A joint estimation problem of the propagation parameters and the 3D virtual environment map is formulated. While the estimation problem is non-convex with degenerated gradient, we discover the partially quasiconvex property, which leads to the development of an efficient parameter estimation radio map construction algorithm. Numerical results demonstrated that by constructing the 3D virtual environment, the required measurement data for achieving a same radio map construction accuracy can be reduced by more than a half. It is also found that when the proposed radio map is applied to UAV placement for UAV-aided relay communication, more than 50% relay capacity gain can be achieved.

APPENDIX A
PROOF OF LEMMA 1

Under $y^{(i)} = \bar{g}(\mathbf{p}^{(i)}; \boldsymbol{\theta}^*, \mathbf{H}^*) + n^{(i)}$, we obtain

$$\begin{aligned} f(\boldsymbol{\theta}, \mathbf{H}) &= \frac{1}{N} \sum_{i=1}^N \left[y^{(i)} - \sum_{k=0}^K (\beta_k + \alpha_k d(\mathbf{p}^{(i)})) S_k(\mathbf{p}^{(i)}; \mathbf{H}) \right]^2 \\ &= \frac{1}{N} \sum_{i=1}^N \left[\bar{g}(\mathbf{p}^{(i)}; \boldsymbol{\theta}^*, \mathbf{H}^*) + n^{(i)} - \sum_{k=0}^K (\beta_k + \alpha_k d(\mathbf{p}^{(i)})) S_k(\mathbf{p}^{(i)}; \mathbf{H}) \right]^2 \\ &= \frac{1}{N} \sum_{i=1}^N \left[(\Delta^{(i)})^2 + 2\Delta^{(i)}n^{(i)} + (n^{(i)})^2 \right] \end{aligned} \quad (17)$$

$$= \bar{f}(\boldsymbol{\theta}, \mathbf{H}) + \frac{1}{N} \sum_{i=1}^N [2\Delta^{(i)}n^{(i)} + (n^{(i)})^2] \quad (18)$$

where, in (17), we denote

$$\Delta^{(i)} = \bar{g}(\mathbf{p}^{(i)}; \boldsymbol{\theta}^*, \mathbf{H}^*) - \sum_{k=0}^K (\beta_k + \alpha_k d(\mathbf{p}^{(i)})) S_k(\mathbf{p}^{(i)}; \mathbf{H})$$

and thus, $\bar{f}(\boldsymbol{\theta}, \mathbf{H}) = \frac{1}{N} \sum_{i=1}^N \Delta^{(i)}$ in (18) as from (7).

It remains to show that the second term in (18) converges to C in probability.

We first show the convergence of $\frac{1}{N} \sum_{i=1}^N 2\Delta^{(i)}n^{(i)}$. For brevity, we denote $X_i = 2\Delta^{(i)}n^{(i)} = 2\Delta^{(i)}(\xi^{(i)} + \tilde{n}^{(i)})$ from the observation model, where we have further denoted $\xi^{(i)} \triangleq \xi(\mathbf{p}^{(i)})$. It follows that $\mathbb{E}\{X_i\} = 0$ since both $\xi^{(i)}$ and $\tilde{n}^{(i)}$ have zero mean. As a result, $\text{cov}(X_i, X_j) = \mathbb{E}\{X_i X_j\} = 4\Delta^{(i)}\Delta^{(j)}\text{cov}(\xi^{(i)}, \xi^{(j)})$ for $i \neq j$, since $\xi^{(i)}$ and $\tilde{n}^{(i)}$ are independent with zero mean.

Note that $\Delta^{(i)}$ is a deterministic function with bounded values due to its definition and the fact that the regions of $\boldsymbol{\theta}$, \mathbf{H} , and $\mathbf{p}^{(i)}$ are bounded, *i.e.*, there exists C_0 , such that $4|\Delta^{(i)}\Delta^{(j)}| <$

C_0 for all i, j . Therefore, we must have $|\text{cov}(X_i, X_j)| \leq C_0 |\text{cov}(\xi^{(i)}, \xi^{(j)})|$ for $i \neq j$. Since $|\text{cov}(\xi^{(i)}, \xi^{(j)})| \rightarrow 0$ as $|i - j| \rightarrow \infty$ and $N \rightarrow \infty$, it follows that $|\text{cov}(X_i, X_j)| \rightarrow 0$.

We are interested in the variance $\mathbb{V}\{\frac{1}{N} \sum_{i=1}^N X_i\}$, which equals to

$$\frac{1}{N^2} \sum_{i=1}^N \mathbb{V}\{X_i\} + \frac{2}{N^2} \sum_{i=1}^N \sum_{j=i+1}^N \text{cov}(X_i, X_j) \quad (19)$$

where, in the first term, $\mathbb{V}\{X_i\} \leq C_1$ since $\xi^{(i)}$ and $\tilde{n}^{(i)}$ have bounded variance and $\Delta^{(i)}$ is bounded. In the second term, the condition $|\text{cov}(X_i, X_j)| \rightarrow 0$ implies that for any $\epsilon_1 > 0$, there exists a finite N_1 such that $\text{cov}(X_i, X_j) < \epsilon_1$ for all $j - i > N_1$. So, it follows that

$$\begin{aligned} \sum_{j=i+1}^N \text{cov}(X_i, X_j) &= \sum_{j=i+1}^{i+N_1} \text{cov}(X_i, X_j) + \sum_{j=i+N_1+1}^N \text{cov}(X_i, X_j) \\ &\leq \sum_{j=i+1}^{i+N_1} \sqrt{\mathbb{V}\{X_i\} \mathbb{V}\{X_j\}} + \sum_{j=i+N_1+1}^N \epsilon_1 \\ &\leq N_1 C_1 + N \epsilon_1 \end{aligned}$$

where the first term in the second line is due to the Cauchy-Schwarz inequality.

As a result, $\mathbb{V}\{\frac{1}{N} \sum_{i=1}^N X_i\}$ from (19) can be upper bounded as

$$\begin{aligned} \mathbb{V}\left\{\frac{1}{N} \sum_{i=1}^N X_i\right\} &\leq \frac{1}{N^2} \sum_{i=1}^N C_1 + \frac{2}{N^2} \sum_{i=1}^N (N_1 C_1 + N \epsilon_1) \\ &= \frac{(1 + 2N_1)C_1}{N} + 2\epsilon_1. \end{aligned}$$

Therefore, for any $\epsilon > 0$, one can choose $\epsilon_1 = \epsilon/3$ and $N_2 = 3(1 + 2N_1)C_1/\epsilon$, such that $\mathbb{V}\{\frac{1}{N} \sum_{i=1}^N X_i\} < \epsilon$ for all $N > N_2$. This establishes that $\mathbb{V}\{\frac{1}{N} \sum_{i=1}^N X_i\} \rightarrow 0$ as $N \rightarrow \infty$.

As a result, by Chebyshev's inequality, we have

$$\mathbb{P}\left\{\left|\frac{1}{N} \sum_{i=1}^N X_i - \mathbb{E}\{X_1\}\right| > \epsilon_0\right\} \leq \frac{\mathbb{V}\{\frac{1}{N} \sum_{i=1}^N X_i\}}{\epsilon_0^2} \rightarrow 0$$

as $N \rightarrow \infty$. This shows that $\frac{1}{N} \sum_{i=1}^N X_i \rightarrow 0$ in probability.

Finally, to show the convergence of $\frac{1}{N} \sum_{i=1}^N (n^{(i)})^2$ in (18), we have

$$\frac{1}{N} \sum_{i=1}^N (n^{(i)})^2 = \frac{1}{N} \sum_{i=1}^N (\tilde{n}^{(i)})^2 + 2\frac{1}{N} \sum_{i=1}^N \tilde{n}^{(i)} \xi^{(i)} + \frac{1}{N} \sum_{i=1}^N (\xi^{(i)})^2$$

where the first term and the second term respectively converges to $\mathbb{E}\{(\tilde{n}^{(i)})^2\} = \sigma_n^2$ and $\mathbb{E}\{\tilde{n}^{(i)} \xi^{(i)}\} = 0$ in probability, as $N \rightarrow \infty$, due to the weak law of large number and the fact that $\tilde{n}^{(i)}$ and $\xi^{(i)}$ are independent;⁵ the third term converges to a finite value C_2 from the assumption of the lemma.

⁵More rigorously, the convergence of the second term can be proven by Chebyshev's inequality following a similar procedure as proving the convergence of $\frac{1}{N} \sum_{i=1}^N X_i$.

Therefore, we have shown that $f(\boldsymbol{\theta}, \mathbf{H}) \rightarrow \bar{f}(\boldsymbol{\theta}, \mathbf{H}) + C$ for $C = \sigma_n^2 + C_2$ in probability as $N \rightarrow \infty$ for every $(\boldsymbol{\theta}, \mathbf{H})$.

APPENDIX B

PROOF OF THEOREM 1

To simplify the notations of the proof, we denote $\gamma_k^{(i)} = \beta_k^* + \alpha_k^* d(\mathbf{p}^{(i)})$ as the path loss for $d(\mathbf{p}^{(i)})$ and the k th degree of signal obstruction, $\mathbb{I}_k^{(i,j)}(\mathbf{h}) = \mathbb{I}\{\mathbf{p}^{(i)} + \boldsymbol{\epsilon}_j \in \mathcal{D}_k(\mathbf{h})\}$, $\forall j = 1, \dots, J-1$, $\mathbb{I}_k^{(i)}(\mathbf{h}) = \mathbb{I}\{\mathbf{p}^{(i)} \in \mathcal{D}_k(\mathbf{h})\}$. Accordingly, $\bar{g}^{(i)} \triangleq \bar{g}(\mathbf{p}^{(i)}; \boldsymbol{\theta}^*, \mathbf{h}^*) = \sum_{k=0}^1 \gamma_k^{(i)} S_k(\mathbf{p}^{(i)}; \mathbf{h}^*)$ from (2), and $S_k(\mathbf{p}^{(i)}; \mathbf{h}^*) = \sum_{j=0}^{J-1} \omega_j \mathbb{I}_k^{(i,j)}(\mathbf{h}^*)$ from (4).

Define variable \mathbf{h}_{-m} as a vector from \mathbf{h} but with the m th element h_m removed. Thus, by restricting $\bar{f}(\boldsymbol{\theta}, \mathbf{h})$ in (7) to take value in the interval \mathcal{I}_m , we have

$$\begin{aligned} \bar{f}_m(h_m; \boldsymbol{\theta}^*, \mathbf{h}_{-m}) &= \frac{1}{N} \sum_{i=1}^N \left[\bar{g}^{(i)} - \sum_{k=0}^1 \gamma_k^{(i)} \sum_{j=0}^{J-1} \omega_j \mathbb{I}_k^{(i,j)}(\mathbf{h}) \right]^2 \\ &= \frac{1}{N} \sum_{i=1}^N \left[\bar{g}^{(i)} - \sum_{k=0}^1 \gamma_k^{(i)} \omega_0 \mathbb{I}_k^{(i)}(\mathbf{h}) - \sum_{k=0}^1 \gamma_k^{(i)} \sum_{j=1}^{J-1} \omega_j \mathbb{I}_k^{(i,j)}(\mathbf{h}) \right]^2. \end{aligned} \quad (20)$$

Substituting $\bar{g}^{(i)}$ into (20), we obtain

$$\begin{aligned} \bar{f}_m(h_m; \boldsymbol{\theta}^*, \mathbf{h}_{-m}) &= \frac{1}{N} \sum_{i=1}^N \left[\sum_{k=0}^1 \gamma_k^{(i)} \omega_0 \mathbb{I}_k^{(i)}(\mathbf{h}^*) - \sum_{k=0}^1 \gamma_k^{(i)} \omega_0 \mathbb{I}_k^{(i)}(\mathbf{h}) \right. \\ &\quad \left. + \sum_{k=0}^1 \gamma_k^{(i)} \sum_{j=1}^{J-1} \omega_j \mathbb{I}_k^{(i,j)}(\mathbf{h}^*) - \sum_{k=0}^1 \gamma_k^{(i)} \sum_{j=1}^{J-1} \omega_j \mathbb{I}_k^{(i,j)}(\mathbf{h}) \right]^2 \\ &= \frac{1}{N} \sum_{i=1}^N \left[\underbrace{\omega_0 \sum_{k=0}^1 \gamma_k^{(i)} (\mathbb{I}_k^{(i)}(\mathbf{h}^*) - \mathbb{I}_k^{(i)}(\mathbf{h}))}_{(a)} + \underbrace{\sum_{j=1}^{J-1} \omega_j \sum_{k=0}^1 \gamma_k^{(i)} (\mathbb{I}_k^{(i,j)}(\mathbf{h}^*) - \mathbb{I}_k^{(i,j)}(\mathbf{h}))}_{(b)} \right]^2. \end{aligned} \quad (21)$$

We have three cases for the value of $\sum_{k=0}^1 \gamma_k^{(i)} (\mathbb{I}_k^{(i)}(\mathbf{h}^*) - \mathbb{I}_k^{(i)}(\mathbf{h}))$ or $\sum_{k=0}^1 \gamma_k^{(i)} (\mathbb{I}_k^{(i,j)}(\mathbf{h}^*) - \mathbb{I}_k^{(i,j)}(\mathbf{h}))$, *i.e.*, 0 , $\gamma_0^{(i)} - \gamma_1^{(i)}$, and $\gamma_1^{(i)} - \gamma_0^{(i)}$. Notice that, $\gamma_0^{(i)} > \gamma_1^{(i)}$ from our model (1) and smaller k means less signal obstruction. $\mathbb{I}_k^{(i,j)}(\mathbf{h}^*) - \mathbb{I}_k^{(i,j)}(\mathbf{h}) \in \{-1, 0, 1\}$.

- For term (a): We have, for both $k = 0$ and 1 , term (a) $\in \{0, \omega_0(\gamma_0^{(i)} - \gamma_1^{(i)}), \omega_0(\gamma_1^{(i)} - \gamma_0^{(i)})\}$.
- For term (b): We obtain a lower bound and an upper bound as

$$\sum_{j=1}^{J-1} \omega_j (\gamma_1^{(i)} - \gamma_0^{(i)}) \leq (b) \leq \sum_{j=1}^{J-1} \omega_j (\gamma_0^{(i)} - \gamma_1^{(i)}). \quad (22)$$

Set $\omega_0 \geq \frac{2}{3}$, it follows that $0 \leq \sum_{j=1}^{J-1} \omega_j \leq \frac{1}{3}$ since $\sum_j \omega_j = 1$, and hence,

$$[\pm \omega_0 + \sum_{j=1}^{J-1} \omega_j]^2 \geq [\sum_{j=1}^{J-1} \omega_j]^2. \quad (23)$$

By (22) and (23), for any i , w.r.t. the value of term (a),

- Substituting the upper bound in (22) into $[(a) + (b)]^2$ in (21), we obtain

$$[\pm\omega_0(\gamma_0^{(i)} - \gamma_1^{(i)}) + \sum_{j=1}^{J-1} \omega_j(\gamma_0^{(i)} - \gamma_1^{(i)})]^2 \geq [0 + \sum_{j=1}^{J-1} \omega_j(\gamma_0^{(i)} - \gamma_1^{(i)})]^2.$$

- Substituting the lower bound in (22) into $[(a) + (b)]^2$ in (21), we obtain

$$[\pm\omega_0(\gamma_0^{(i)} - \gamma_1^{(i)}) + \sum_{j=1}^{J-1} \omega_j(\gamma_1^{(i)} - \gamma_0^{(i)})]^2 \geq [0 + \sum_{j=1}^{J-1} \omega_j(\gamma_1^{(i)} - \gamma_0^{(i)})]^2.$$

Hence,

$$\begin{aligned} & [\pm\omega_0(\gamma_0^{(i)} - \gamma_1^{(i)}) + \sum_{j=1}^{J-1} \omega_j \sum_{k=0}^1 \gamma_k^{(i)} (\mathbb{I}_k^{(i,j)}(\mathbf{h}^*) - \mathbb{I}_k^{(i,j)}(\mathbf{h}))]^2 \\ & \geq [0 + \sum_{j=1}^{J-1} \omega_j \sum_{k=0}^1 \gamma_k^{(i)} (\mathbb{I}_k^{(i,j)}(\mathbf{h}^*) - \mathbb{I}_k^{(i,j)}(\mathbf{h}))]^2 \quad (24) \end{aligned}$$

where $\pm\omega_0(\gamma_0^{(i)} - \gamma_1^{(i)})$ is for $\mathbb{I}_k^{(i)}(\mathbf{h}^*) \neq \mathbb{I}_k^{(i)}(\mathbf{h})$ and 0 is for $\mathbb{I}_k^{(i)}(\mathbf{h}^*) = \mathbb{I}_k^{(i)}(\mathbf{h})$ in term (a).

Denote the right hand side in (24) as $A^{(i)}$, the left hand side as $B^{(i)}$, and two sets $\mathcal{I}_A(\mathbf{h}) = \{i \mid \mathbb{I}_k^{(i)}(\mathbf{h}) = \mathbb{I}_k^{(i)}(\mathbf{h}^*)\}$, $\mathcal{I}_B(\mathbf{h}) = \{i \mid \mathbb{I}_k^{(i)}(\mathbf{h}) \neq \mathbb{I}_k^{(i)}(\mathbf{h}^*)\} = \{1, 2, \dots, N\} \setminus \mathcal{I}_A(\mathbf{h})$.

Recall the obstacle indicator function in (3)

$$\mathbb{I}\{\mathbf{p}^{(i)} \in \mathcal{D}_k(\mathbf{H})\} = (1 - \prod_{j \in \mathcal{B}^{(i)}} (1 - \mathbb{I}\{h_{j,k} \geq z_j^{(i)}\})) \prod_{j \in \mathcal{B}^{(i)} l > k} \prod \mathbb{I}\{h_{j,l} < z_j^{(i)}\}$$

and we denote a set

$$\mathcal{L}_m(\mathbf{h}) = \left\{ i \mid h_j < z_j^{(i)}, \forall j \in \mathcal{B}^{(i)} \setminus \{m\} \right\}$$

as measurement samples that can only be blocked by m th grid. Then, w.r.t. h_m , values of $\mathbb{I}_k^{(i)}(\mathbf{h})$ have two types: (i) dependent of h_m , i.e., index $i \in \mathcal{L}_m(\mathbf{h})$, and by the condition $h_j^* < h_j$ and $h_j < z_j^{(i)}, \forall j \in \mathcal{B}^{(i)} \setminus \{m\}$,

$$\mathbb{I}_k^{(i)}(h_m; \mathbf{h}_{-m}) = (1 - (1 - \mathbb{I}\{h_{m,k} \geq z_{m,k}^{(i)}\})) \prod_{l > k} \mathbb{I}\{h_{m,l} < z_m^{(i)}\}$$

so $\mathbb{I}_0^{(i)}(h_m; \mathbf{h}_{-m}) = \mathbb{I}\{h_m < z_m^{(i)}\} = \mathbb{I}_0^{(i)}(h_m; \mathbf{h}_{-m}^*)$ and $\mathbb{I}_1^{(i)}(h_m; \mathbf{h}_{-m}) = \mathbb{I}\{h_m \geq z_m^{(i)}\} = \mathbb{I}_1^{(i)}(h_m; \mathbf{h}_{-m}^*)$; (ii) independent of h_m , i.e., index $i \in \{1, 2, \dots, N\} \setminus \mathcal{L}_m(\mathbf{h})$, and then $\mathbb{I}_k^{(i)}(h_m; \mathbf{h}_{-m})$ will be constant. Hence, we only need to consider the type (i) samples. For index $i \in \mathcal{L}_m(\mathbf{h})$,

- LOS measurement samples satisfy $h_m^* < z_m^{(i)}$. As shown in Fig. 7, when $h_m < z_m^{(i)}$, we obtain $\mathbb{I}_k^{(i)}(\mathbf{h}) = \mathbb{I}_k^{(i)}(\mathbf{h}^*)$ and $[(a) + (b)]^2$ in (21) taking value $A^{(i)}$. When $h_m \geq z_m^{(i)}$, we obtain $\mathbb{I}_k^{(i)}(\mathbf{h}) \neq \mathbb{I}_k^{(i)}(\mathbf{h}^*)$ and $[(a) + (b)]^2$ taking value $B^{(i)}$.

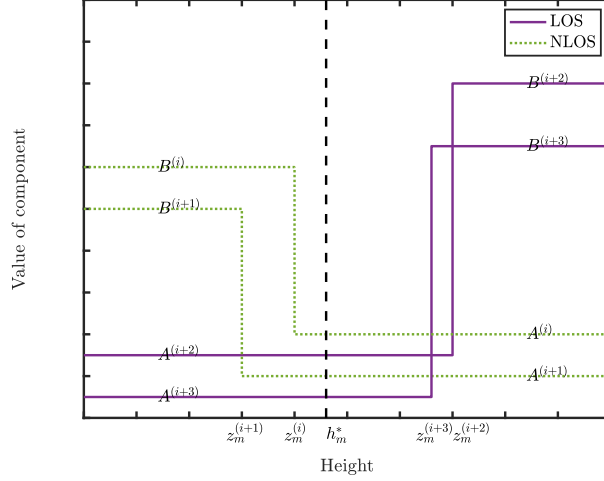


Figure 7. An example for the value of component $[\bar{g}^{(i)} - \sum_{k=0}^1 \gamma_k^{(i)} \sum_{j=0}^{J-1} \omega_j \mathbb{I}_k^{(i,j)}(\mathbf{h})]^2$ vs. h_m .

- NLOS measurement samples satisfy $h_m^* \geq z_m^{(i)}$. As shown in Fig. 7, when $h_m \geq z_m^{(i)}$, we obtain $\mathbb{I}_k^{(i)}(\mathbf{h}) = \mathbb{I}_k^{(i)}(\mathbf{h}^*)$ and $[(a) + (b)]^2$ in (21) taking value $A^{(i)}$. When $h_m < z_m^{(i)}$, we obtain $\mathbb{I}_k^{(i)}(\mathbf{h}) \neq \mathbb{I}_k^{(i)}(\mathbf{h}^*)$ and $[(a) + (b)]^2$ taking value $B^{(i)}$.

Therefore, the smaller the distance between h_m and h_m^* is, the larger the set $\mathcal{I}_A(h_m; \mathbf{h}_{-m})$ will be, *i.e.*, the more $\mathbb{I}_k^{(i)}(h_m; \mathbf{h}_{-m}) = \mathbb{I}_k^{(i)}(h_m^*; \mathbf{h}_{-m}^*)$. $\forall \epsilon > 0$, when $h_m < h_m^*$, $\mathcal{I}_A(h_m - \epsilon; \mathbf{h}_{-m}) \subseteq \mathcal{I}_A(h_m; \mathbf{h}_{-m})$, and when $h_m > h_m^*$, $\mathcal{I}_A(h_m + \epsilon; \mathbf{h}_{-m}) \subseteq \mathcal{I}_A(h_m; \mathbf{h}_{-m})$. Intuitively, for index $i \in \mathcal{L}_m(\mathbf{h})$, the value of $[(a) + (b)]^2$ in (21) is shown in Fig. 7, and for index $i \in \{1, 2, \dots, N\} \setminus \mathcal{L}_m(\mathbf{h})$, the value is constant in h_m . We can see the summation of all LOS is increasing in h_m and is constant from zero to a height which is greater than h_m^* . Similarly, the summation of all NLOS is decreasing in h_m and is constant from zero to a height which is less than h_m^* , so the summation of all LOS and NLOS is quasiconvex. Then, we will show the relation between the sets and the function value mathematically.

$$\bar{f}_m(h_m; \boldsymbol{\theta}^*, \mathbf{h}_{-m}) = \sum_{i \in \mathcal{I}_A(\mathbf{h})} A^{(i)} + \sum_{i \in \mathcal{I}_B(\mathbf{h})} B^{(i)}$$

where $0 < A^{(i)} \leq B^{(i)}$. $\forall \epsilon > 0$, when $\forall h_m < h_m^*$, by using $\mathcal{I}_A(h_m - \epsilon; \mathbf{h}_{-m}) \subseteq \mathcal{I}_A(h_m; \mathbf{h}_{-m})$ and $\mathcal{I}_A(h_m; \mathbf{h}_{-m}) = \{1, 2, \dots, N\} \setminus \mathcal{I}_A(h_m; \mathbf{h}_{-m})$, we finally have

$$\bar{f}_m(h_m - \epsilon; \boldsymbol{\theta}^*, \mathbf{h}_{-m}) \geq \bar{f}_m(h_m; \boldsymbol{\theta}^*, \mathbf{h}_{-m}).$$

Similarly, $\forall \epsilon > 0$, when $\forall h_m > h_m^*$,

$$\bar{f}_m(h_m + \epsilon; \boldsymbol{\theta}^*, \mathbf{h}_{-m}) \geq \bar{f}_m(h_m; \boldsymbol{\theta}^*, \mathbf{h}_{-m}).$$

To sum up, $\bar{f}_m(h_m; \boldsymbol{\theta}^*; \mathbf{h}_{-m})$ is quasiconvex in h_m .

APPENDIX C

PROOF OF THEOREM 2

By Theorem 1, we already have $\bar{f}_{m,1}(h_{m,1}; \boldsymbol{\theta}^*, \mathbf{H}_{m,1}^-)$ is quasiconvex under the given condition, where $\mathbf{H}_{m,k}^-$ is a matrix representing \mathbf{H} removing $h_{m,k}$. Then, we generalize the proof to $K > 1$, when $S_k(\mathbf{p}^{(i)}; \mathbf{H})$ is chosen as the indicator function, *i.e.*, $\omega_0 = 1$. As mentioned previously, $\forall m$, given $\mathbf{H}_{m,1}^- \succeq \mathbf{H}_{m,1}^-$ and obstacle indicator function (3), values of $\mathbb{I}_k^{(i)}(\mathbf{H})$ have two types: (i) $\mathbb{I}_0^{(i)}(\mathbf{H}) = \mathbb{I}\{h_{m,1} < z_m^{(i)}\}$, $\mathbb{I}_1^{(i)}(\mathbf{H}) = \mathbb{I}\{h_{m,1} \geq z_m^{(i)}\}$; (ii) independent of $h_{m,1}$. The case (i) is also known as measurement samples which can only be blocked by m th grid and denote it as

$$\mathcal{L}_{m,K}(\mathbf{H}) = \left\{ i \mid h_{j,K} < z_{j,K}^{(i)}, \forall j \in \mathcal{B}^{(i)} \setminus \{m\} \right\} \quad (25)$$

where $K = 1$. In a general $K > 1$ case, we denote a set $\mathcal{L}_{m,k}(\mathbf{H})$ for samples only blocked by m th grid and no more obstructed than k th class obstacle

$$\mathcal{L}_{m,k}(\mathbf{H}) = \left\{ i \mid h_{j,l} < z_j^{(i)}, \forall l \geq k, \forall j \in \mathcal{B}^{(i)} \setminus \{m\} \right\}.$$

For quasiconvex of NLOS obstacle, *i.e.*, obstacle of the most obscured propagation, we can similarly follow the pipeline of previous $K = 1$ situation, function (7) becomes

$$\bar{f}_{m,K}(h_{m,K}; \boldsymbol{\theta}^*, \mathbf{H}_{m,k}^-) = \frac{1}{N} \sum_{i=1}^N [\bar{g}^{(i)} - \sum_{k=0}^K \gamma_k^{(i)} \mathbb{I}_k^{(i)}(\mathbf{H})]^2. \quad (26)$$

Recall that $\bar{g}^{(i)} = \sum_{k=0}^K \gamma_k^{(i)} \mathbb{I}_k^{(i)}(\mathbf{H}^*)$ is from (2), and we denote $\gamma_k^{(i)} = \beta_k^* + \alpha_k^* d(\mathbf{p}^{(i)})$ as the path loss for $d(\mathbf{p}^{(i)})$ and the k th degree of signal obstruction, $\mathbb{I}_k^{(i)}(\mathbf{H}) = \mathbb{I}\{\mathbf{p}^{(i)} \in \mathcal{D}_k(\mathbf{H})\}$. Substitute $\bar{g}^{(i)}$ into (26). We obtain

$$\begin{aligned} \bar{f}(h_{m,K}; \boldsymbol{\theta}^*, \mathbf{H}_{m,k}^-) &= \frac{1}{N} \sum_{i=1}^N \left[\sum_{k=0}^K \gamma_k^{(i)} \mathbb{I}_k^{(i)}(\mathbf{H}^*) - \sum_{k=0}^K \gamma_k^{(i)} \mathbb{I}_k^{(i)}(\mathbf{H}) \right]^2 \\ &= \frac{1}{N} \sum_{i=1}^N \left[\sum_{k=0}^K \gamma_k^{(i)} (\mathbb{I}_k^{(i)}(\mathbf{H}^*) - \mathbb{I}_k^{(i)}(\mathbf{H})) \right]^2. \end{aligned}$$

For term $\sum_{k=0}^K \gamma_k^{(i)} (\mathbb{I}_k^{(i)}(\mathbf{H}^*) - \mathbb{I}_k^{(i)}(\mathbf{H}))$ in it: We have

$$\sum_{k=0}^K \gamma_k^{(i)} (\mathbb{I}_k^{(i)}(\mathbf{H}^*) - \mathbb{I}_k^{(i)}(\mathbf{H})) = \begin{cases} A^{(i)}, & \text{if } \mathbb{I}_k^{(i)}(\mathbf{H}^*) = \mathbb{I}_k^{(i)}(\mathbf{H}), \\ B^{(i)}, & \text{if } \mathbb{I}_k^{(i)}(\mathbf{H}^*) \neq \mathbb{I}_k^{(i)}(\mathbf{H}). \end{cases}$$

where $A^{(i)} = 0$ and $B^{(i)} \neq 0$. Denote two sets $\mathcal{I}_A(\mathbf{H}) = \{i \mid \mathbb{I}_k^{(i)}(\mathbf{H}) = \mathbb{I}_k^{(i)}(\mathbf{H}^*)\}$, $\mathcal{I}_B(\mathbf{H}) = \{i \mid \mathbb{I}_k^{(i)}(\mathbf{H}) \neq \mathbb{I}_k^{(i)}(\mathbf{H}^*)\} = \{1, 2, \dots, N\} \setminus \mathcal{I}_A(\mathbf{H})$ and similar to the proof of Theorem 1, the smaller the distance between $h_{m,K}$ and $h_{m,K}^*$ is, the larger the set $\mathcal{I}_A(h_{m,K}; \mathbf{H}_{m,k}^-)$ will be, *i.e.*, the more $\mathbb{I}_k^{(i)}(h_{m,K}; \mathbf{H}_{m,k}^-) = \mathbb{I}_k^{(i)}(h_{m,K}^*; \mathbf{H}_{m,k}^-)$. Therefore, $\bar{f}_{m,K}(h_{m,K}; \boldsymbol{\theta}^*, \mathbf{H}_{m,k}^-)$ is

quasiconvex in $h_{m,K}$. We have the sets $\mathcal{L}_{m,K}(\mathbf{H})$ and class- K obstacle heights $h_{m,K}$, where $m = 1, 2, \dots, M$. Followed by NLOS obstacle, the obstacle of less obscured propagation is class- $K - 1$ and the set is

$$\mathcal{L}_{m,K-1}(\mathbf{H}) = \left\{ i \mid h_{j,l} < z_j^{(i)}, \forall l \geq K - 1, \forall j \in \mathcal{B}^{(i)} \setminus \{m\} \right\}$$

in which $l = K - 1, K$. On the condition of the sets $\mathcal{L}_{m,K}(\mathbf{H})$ and class- K obstacle heights $h_{m,K}$, $\mathcal{L}_{m,K-1}(\mathbf{H})$ can be also written as

$$\mathcal{L}_{m,K-1}(\mathbf{H}) = \left\{ i \mid h_{j,K-1} < z_j^{(i)}, \forall j \in \mathcal{B}^{(i)} \setminus \{m\} \right\} \cap \mathcal{L}_{m,K}(\mathbf{H})$$

which is now also similar to the previous situation (25). In other words, when we have the most obscured propagation situation, the less obscured propagation situation can be recursively get. As a result, for all m, k , quasiconvexity of $\bar{f}_{m,k}(h_{m,k}; \boldsymbol{\theta}^*, \mathbf{H}_{m,k}^-)$ is proved and then $\bar{f}(\boldsymbol{\theta}^*, \mathbf{H})$ is element-wise quasiconvex for each individual element $h_{m,k}$.

APPENDIX D

PROOF OF THEOREM 3

First of all, the optimal solution \mathcal{H}^* to minimize function (7) are intervals, because in the objective function, variable \mathbf{H} is only in an indicator function taking 1 by comparing the range of those values. Denote \mathcal{M}_m as the index set of measurements $(\mathbf{p}^{(i)}, y^{(i)})$ that the link $(\mathbf{p}_u^{(i)}, \mathbf{p}_d^{(i)})$ passes over the m th grid cell. Then, by the proof of Theorem 2, similar to $\mathcal{L}_{m,k}(\mathbf{H})$, denote a set $\mathcal{Q}_{m,k}(\mathbf{H})$ for samples passing m th grid and no more obstructed than k th class obstacle, *i.e.*,

$$\mathcal{Q}_{m,k}(\mathbf{H}) = \left\{ i \mid h_{j,l} < z_j^{(i)}, \forall l \geq k, \forall j \in \mathcal{B}^{(i)}, \forall i \in \mathcal{M}_m \right\} \quad (27)$$

and the optimal set $\mathcal{Q}_{m,k}(\mathbf{H}^*)$

$$\mathcal{Q}_{m,k}(\mathbf{H}^*) = \left\{ i \mid h_{j,l}^* < z_j^{(i)}, \forall l \geq k, \forall j \in \mathcal{B}^{(i)}, \forall i \in \mathcal{M}_m \right\}$$

So it follows that $\mathcal{Q}_{m,1}(\mathbf{H}) \subseteq \mathcal{Q}_{m,2}(\mathbf{H}) \subseteq \dots \subseteq \mathcal{Q}_{m,K}(\mathbf{H}), \forall m, K > 1$. Recall the obstacle indicator function in (3), then it is obvious that $h_{m,1} \geq h_{m,2} \geq \dots \geq h_{m,K}, \forall m, K > 1$. Given the condition that $\mathbf{H}' \succeq \mathbf{H}^*$, we thus have

$$\mathcal{Q}_{m,k}(\mathbf{H}') \subseteq \mathcal{Q}_{m,k}(\mathbf{H}^*), \forall m, k. \quad (28)$$

From the proof of Theorem 2 and Fig. 7, denote the k th class obstacle height estimation of m th grid

$$\begin{aligned} \hat{h}_{m,k} &= \sup \arg \min_{h_{m,k}} \bar{f}_{m,k}(h_{m,k}; \boldsymbol{\theta}^*, \mathbf{H}_{m,k}^-) \\ &= \min(z_m^{(i)}), i \in \mathcal{Q}_{m,k}(\mathbf{H}'). \end{aligned} \quad (29)$$

Therefore, by (28)–(29),

$$\begin{aligned}\hat{h}_{m,k} &= \min(z_m^{(i)}), i \in \mathcal{Q}_{m,k}(\mathbf{H}') \\ &\geq \min(z_m^{(i)}), i \in \mathcal{Q}_{m,k}(\mathbf{H}^*) = h_{m,k}^*.\end{aligned}$$

Similarly, for $k = K, K - 1, \dots, 1$ and for all m , we have the same results, so we can have $\hat{\mathbf{H}} \succeq \mathbf{H}^*$.

As for the $\hat{h}_{m,k}(\boldsymbol{\theta}^*, \mathbf{H}'') \geq \hat{h}_{m,k}(\boldsymbol{\theta}^*, \mathbf{H}')$ under $\mathbf{H}'' \succeq \mathbf{H}' \succeq \mathbf{H}^*$: When \mathbf{H}' taking value of $\mathbf{1}H_{\max}$, \mathbf{H}'' can only equal to $\mathbf{1}H_{\max}$ and

$$\begin{aligned}\hat{h}_{m,k}(\boldsymbol{\theta}^*, \mathbf{H}') &= \min(z_m^{(i)}), i \in \mathcal{Q}_{m,k}(\mathbf{1}H_{\max}) \\ &= \hat{h}_{m,k}(\boldsymbol{\theta}^*, \mathbf{H}'')\end{aligned}$$

so $\hat{h}_{m,k}(\boldsymbol{\theta}^*, \mathbf{H}'') \geq \hat{h}_{m,k}(\boldsymbol{\theta}^*, \mathbf{H}')$ and $H_{\max} \geq \hat{h}_{m,k}(\boldsymbol{\theta}^*, \mathbf{H}')$. For arbitrary \mathbf{H}' , when $\mathbf{H}'' \succeq \mathbf{H}' \succeq \mathbf{H}^*$ is satisfied, by (27) $\mathcal{Q}_{m,k}(\mathbf{H}'') \subseteq \mathcal{Q}_{m,k}(\mathbf{H}')$ and similar to (29)

$$\begin{aligned}\hat{h}_{m,k}(\boldsymbol{\theta}^*, \mathbf{H}'') &= \min(z_m^{(i)}), i \in \mathcal{Q}_{m,k}(\mathbf{H}'') \\ &\geq \min(z_m^{(i)}), i \in \mathcal{Q}_{m,k}(\mathbf{H}') = \hat{h}_{m,k}(\boldsymbol{\theta}^*, \mathbf{H}')\end{aligned}$$

thus it always holds.

REFERENCES

- [1] Y.-G. Lim, Y. J. Cho, M. S. Sim, Y. Kim, C.-B. Chae, and R. A. Valenzuela, "Map-based millimeter-wave channel models: An overview, data for B5G evaluation and machine learning," *IEEE Wireless Commun.*, vol. 27, no. 4, pp. 54–62, 2020.
- [2] X. Mo, Y. Huang, and J. Xu, "Radio-map-based robust positioning optimization for UAV-enabled wireless power transfer," *IEEE Wireless Commun. Lett.*, vol. 9, no. 2, pp. 179–183, 2019.
- [3] S. Zhang and R. Zhang, "Radio map based 3D path planning for cellular-connected UAV," *IEEE Trans. on Wireless Commun.*, 2020.
- [4] O. Esrafilian, R. Gangula, and D. Gesbert, "3D map-based trajectory design in UAV-aided wireless localization systems," *IEEE Internet of Things Journal*, 2020.
- [5] Y. Zeng and X. Xu, "Toward environment-aware 6G communications via channel knowledge map," *IEEE Wireless Commun.*, vol. 28, no. 3, pp. 84–91, 2021.
- [6] X. Xia, Y. Wang, K. Xu, Y. Xu, and W. Xie, "Toward digitalizing the wireless environment: A unified A2G information and energy delivery framework based on binary channel feature map," *IEEE Trans. Wireless Commun.*, vol. 21, no. 8, pp. 6448–6463, 2022.
- [7] Y. Zeng, X. Xu, S. Jin, and R. Zhang, "Simultaneous navigation and radio mapping for cellular-connected UAV with deep reinforcement learning," *IEEE Trans. Wireless Commun.*, vol. 20, no. 7, pp. 4205–4220, 2021.
- [8] Q. Hu, Y. Cai, A. Liu, G. Yu, and G. Y. Li, "Low-complexity joint resource allocation and trajectory design for UAV-aided relay networks with the segmented ray-tracing channel model," *IEEE Trans. on Wireless Commun.*, vol. 19, no. 9, pp. 6179–6195, 2020.

- [9] A. Al-Hourani, S. Kandeepan, and A. Jamalipour, "Modeling air-to-ground path loss for low altitude platforms in urban environments," in *Proc. IEEE Global Telecomm. Conf.*, Austin, TX, USA, Dec. 2014.
- [10] C. You and R. Zhang, "Hybrid offline-online design for UAV-enabled data harvesting in probabilistic LoS channel," *IEEE Trans. on Wireless Commun.*, vol. 19, no. 6, pp. 3753–3768, 2020.
- [11] Q. Jiang, Y. Ma, K. Liu, and Z. Dou, "A probabilistic radio map construction scheme for crowdsourcing-based fingerprinting localization," *IEEE Sensors Journal*, vol. 16, no. 10, pp. 3764–3774, 2016.
- [12] Y. Zhang and L. Ma, "Radio map crowdsourcing update method using sparse representation and low rank matrix recovery for WLAN indoor positioning system," *IEEE Wireless Commun. Lett.*, 2021.
- [13] K. S. Ni and T. Q. Nguyen, "Adaptable K-nearest neighbor for image interpolation," in *Proc. IEEE Int. Conf. Acoustics, Speech, and Signal Processing*, Las Vegas, NV, USA, Mar. 2008.
- [14] R. Deng, Z. Jiang, S. Zhou, S. Cui, and Z. Niu, "A two-step learning and interpolation method for location-based channel database construction," in *Proc. IEEE Global Telecommu. Conf.*, Abu Dhabi, United Arab, Dec. 2018.
- [15] H. Braham, S. B. Jemaa, G. Fort, E. Moulines, and B. Sayrac, "Fixed rank Kriging for cellular coverage analysis," *IEEE Trans. on Veh. Technol.*, vol. 66, no. 5, pp. 4212–4222, 2016.
- [16] K. Sato and T. Fujii, "Kriging-based interference power constraint: Integrated design of the radio environment map and transmission power," *IEEE Trans. on Cognitive Commun. and Networking*, vol. 3, no. 1, pp. 13–25, 2017.
- [17] U. Masood, H. Farooq, and A. Imran, "A machine learning based 3D propagation model for intelligent future cellular networks," in *Proc. IEEE Global Commun. Conf.*, Waikoloa, HI, USA, USA, Dec. 2019.
- [18] A. Massa, D. Marcantonio, X. Chen, M. Li, and M. Salucci, "DNNs as applied to electromagnetics, antennas, and propagation—A review," *IEEE Antennas Wireless Propag. Lett.*, vol. 18, no. 11, pp. 2225–2229, 2019.
- [19] Y. Teganya and D. Romero, "Deep completion autoencoders for radio map estimation," vol. 21, no. 3, pp. 1710–1724, 2021.
- [20] R. Levie, Ç. Yapar, G. Kutyniok, and G. Caire, "RadioUNet: Fast radio map estimation with convolutional neural networks," *IEEE Trans. Wireless Commun.*, vol. 20, pp. 4001–4015, 2021.
- [21] S. Shrestha, X. Fu, and M. Hong, "Deep spectrum cartography: Completing radio map tensors using learned neural models," vol. 70, pp. 1170–1184, 2022.
- [22] C. Fan, X. Zhong, and J. Wei, "BS-to-ground channel reconstruction with 3D obstacle map based on RSS measurements," *IEEE Access*, vol. 7, pp. 99 633–99 641, 2019.
- [23] O. Esrafilian, R. Gangula, and D. Gesbert, "Map reconstruction in UAV networks via fusion of radio and depth measurements," in *Proc. IEEE Int. Conf. Commun.*, Montreal, QC, Canada, Jun. 2021.
- [24] A. Eleryan, M. Elsabagh, and M. Youssef, "Synthetic generation of radio maps for device-free passive localization," in *Proc. IEEE Global Telecommu. Conf.*, Houston, TX, USA, USA, Dec. 2011.
- [25] N. Suga, R. Sasaki, M. Osawa, and T. Furukawa, "Ray tracing acceleration using total variation norm minimization for radio map simulation," *IEEE Wireless Commun. Lett.*, 2020.
- [26] J. Chen, U. Yatnalli, and D. Gesbert, "Learning radio maps for UAV-aided wireless networks: A segmented regression approach," in *Proc. IEEE Int. Conf. Commun.*, Paris, France, May 2017.
- [27] J. Chen, O. Esrafilian, D. Gesbert, and U. Mitra, "Efficient algorithms for air-to-ground channel reconstruction in UAV-aided communications," in *Proc. IEEE Global Telecomm. Conf.*, Singapore, Dec. 2017, Wi-UAV workshop.
- [28] B. Zhang and J. Chen, "Constructing radio maps for UAV communications via dynamic resolution virtual obstacle maps," in *Proc. Int. Workshop on Signal Process. Adv. in Wireless Commun.*, Atlanta, GA, USA, May 2020.
- [29] S. M. Kay, *Fundamentals of statistical signal processing*. Prentice Hall PTR, 1993.
- [30] J. Fan, *Local polynomial modelling and its applications: Monographs on statistics and applied probability 66*. Routledge, 1996.